# Synthesis, Structure, and Electrochemical Behaviour of O3-type $NaNi_{1/3}Mn_{1/3}Al_{1/3}O_2$

Neha Dagar<sup>1</sup>, Samriddhi Saxena<sup>1</sup>, Sonia Deswal<sup>2</sup>, Pradeep Kumar<sup>2</sup>, Karthik Chinnathambi<sup>3</sup>, and Sunil Kumar<sup>1,\*</sup>

<sup>1</sup>Department of Metallurgical Engineering and Materials Science, Indian Institute of Technology Indore, Simrol, 453552, India

<sup>2</sup>School of Physical Sciences, Indian Institute of Technology Mandi, Mandi, 175005, India <sup>3</sup>Micron School of Materials Science and Engineering, Boise State University, Boise, ID 83725, USA

\*sunil@iiti.ac.in

#### **Abstract**

O3-type layered oxides are being actively investigated as potential positive electrodes for Naion batteries due to their high specific capacity. In this work, the role of synthesis conditions on the phase formation in NaNi<sub>1/3</sub>Mn<sub>1/3</sub>Al<sub>1/3</sub>O<sub>2</sub> (NMA111) sample was investigated, and an O3-type phase  $(R\bar{3}m)$ , along with a minor  $\beta$ -phase  $(Pn2_1a)$ , was obtained in the pellet (covered with a sacrificial powder) heated at 850 °C. NMA111 exhibited a mixed conducting behaviour at room temperature, with ionic and electronic conductivities estimated to be  $\sim 5.82 \times 10^{-6}$  S cm<sup>-1</sup> and  $\sim 2.15 \times 10^{-6}$  S cm<sup>-1</sup>, respectively. The oxidation states and local structure of Mn and Ni were confirmed by X-ray photoelectron spectroscopy (XPS) and X-ray absorption spectroscopy studies. The electrochemical behaviour of NMA111 was also investigated using the GCD, CV, GITT, and in-situ EIS techniques. The cathode showed an initial discharge capacity of ~87 mAh g<sup>-1</sup> (which corresponds to 0.33 Na-ions reversible intercalation) at 0.1C in the 2.0 to 4.0 V range, and the voltage profile suggested a solid-solution type insert mechanism. A discharged capacity of 70 mAh g<sup>-1</sup> at 2C (~80 % of the initial capacity at 0.1C), and a capacity retention of 70% after 100 cycles at 0.3C were obtained in the NMA111 cathode. The ex-situ XPS measurements confirmed that the Ni<sup>2+/3+</sup> redox couple is responsible for the charge compensation in NMA111 during the charge-discharge process.

**Keywords**: Cathode materials; Na-ion batteries; Layered oxides; Electrochemical properties

#### 1 Introduction

Na-ion batteries (NIBs), which have a working mechanism similar to Li-ion batteries (LIBs), have attracted considerable attention from academia and industry due to the abundance of sodium precursors [1-3]. Nevertheless, limitations in the specific energy and rate performance of Na-ion batteries arise from the heavier Na-ion and lower electrode potential of Na/Na<sup>+</sup>. Accordingly, a lot of research focus has been on developing novel cathode compositions [4-7]. Sodium transition metal oxides, with the general formula Na<sub>x</sub>MO<sub>2</sub> (M is typically a combination of redox-active elements), are especially attractive due to their flexibility in accommodating various cations at transition metal sites and varied Na content in the Na-O2 layers [8-10]. The compositional diversity in these materials also leads to the formation of various phases, classified in P and O types depending on the coordination of the sodium cation in the crystal structure. While P2-type layered oxides offer fast Na-ion transport due to the larger bottleneck area of prismatic sites, O3-type phases have the important advantage of having comparatively higher specific capacity due to the higher initial Na content in the structure (*x* is often 1) [11-13].

During the charge-discharge process, the removal of Na-ions from the O3-type crystal structure creates an increasing number of prismatic vacancies, which often lead to a series of complex phase transitions. These transitions are caused by Na-ions/vacancies ordering, the Jahn-Teller distortion, transition metal ordering, sliding of the MO2 layers, migration of transition metal ions, etc., and often involve large volume changes and may even be irreversible [14-16]. The resultant structural instability causes capacity degradation and adverse effects on the cycling performance of O3 cathodes. Substitution and doping of different elements at the M and Na sites have been shown to be effective in alleviating some of these adverse issues [17-23]. In general, binary and ternary metal systems (i.e., 2 and 3 metal cations at the M site) have better electrochemical performance than corresponding unary systems. For instance, the presence of Ni in the Na<sub>x</sub>MnO<sub>2</sub> system (both as P2- Na<sub>0.67</sub>Mn<sub>0.67</sub>Ni<sub>0.33</sub>O<sub>2</sub> or O3- NaMn<sub>0.5</sub>Ni<sub>0.5</sub>O<sub>2</sub>) improves the cyclability and average discharge voltage [24-29].

Recently, there has been a focus on incorporating multiple cations in the transition metal layers [30, 31]. The random distribution of these cations at the Wyckoff position introduces an increase in configurational entropy. The enhanced entropy and mixed cation doping effect create charge disorder that suppresses the Na<sup>+</sup>/vacancy and honeycomb ordering, as well as facilitates the faster Na diffusion [32-36]. Al doping has been demonstrated to enhance the electrochemical performance of various sodium-layered oxide cathodes. For instance, in the

compound NaNi<sub>1/3</sub>Mn<sub>1/3-x</sub>Fe<sub>1/3</sub>Al<sub>x</sub>O<sub>2</sub>, 0.5% Al substitution led to an initial discharge capacity of 115.1 mAh g<sup>-1</sup> at 1C, and an impressive capacity retention of ~88% after 200 cycles [37]. Similarly, Na(Ni<sub>1/3</sub>Mn<sub>1/3</sub>Fe<sub>1/3</sub>)<sub>0.95</sub>Al<sub>0.05</sub>O<sub>2</sub> cathode showed an initial capacity of 145.4 mAh g<sup>-1</sup> at 0.1 C, with a reversible capacity of 128.4 mAh g<sup>-1</sup> after 80 cycles at 0.2 C [38]. Al doping in Na<sub>0.67</sub>Al<sub>0.10</sub>Fe<sub>0.05</sub>Mn<sub>0.85</sub>O<sub>2</sub> also resulted in an exceptional initial capacity of 202 mAh g<sup>-1</sup> in the 2.0-4.0 V range, 81% capacity retention after 600 cycles, and good rate performance with capacities reaching 122 mAh g<sup>-1</sup> at 1200 mA g<sup>-1</sup> [39]. Further, Al incorporation in Na<sub>0.75</sub>(Mn,Ni)O<sub>2</sub> showed improved rate performance, better cyclability, and suppression of phase transitions in P2 and P3 phases [17, 40]. These studies have shown that the presence of earth-abundant Al in layered oxides improves cyclability and rate performance by stabilizing the structure and modifying the interlayer spacings. However, stabilizing the O3-type phase remains challenging because of sodium volatilization and competing P2-phase formation during high-temperature synthesis.

This study explored the synthesis and characterization of a promising O3-type  $NaNi_{1/3}Mn_{1/3}Al_{1/3}O_2$  layered oxide (denoted hereafter as NMA111). The crystal structure of the sample was elucidated by the Rietveld refinement of X-ray diffraction (XRD) data, selected area electron diffraction pattern (SAED), and high-resolution transmission electron microscopy (HRTEM). The calcination conditions were found to greatly affect the nature of the phase(s) formed. NMA111 exhibited a reversible specific capacity of ~87 mAh g<sup>-1</sup> at 0.1C, which was attributed to the  $Ni^{2+/3+}$  charge compensation.

## 2 Experimental Section

## 2.1 Synthesis of NMA111

Layered oxide with the nominal stoichiometry of NaNi<sub>1/3</sub>Mn<sub>1/3</sub>Al<sub>1/3</sub>O<sub>2</sub> was prepared by the sol–gel method using NaNO<sub>3</sub>, C<sub>4</sub>H<sub>6</sub>MnO<sub>4</sub>·4H<sub>2</sub>O, C<sub>4</sub>H<sub>6</sub>NiO<sub>4</sub>·4H<sub>2</sub>O, and Al(NO<sub>3</sub>)<sub>3</sub>·9H<sub>2</sub>O as precursors in the molar ratio 1:0.333:0.333:0.333; respectively. The precursors were dissolved in deionized water (DI) and stirred using a magnetic stirrer for homogeneous mixing. Ethylene glycol and citric acid were added (molar ratio 1:2) to the solutions to form a gel, followed by drying the gel by heating it at 120 °C. The resultant 10 g powder was heated at 650 °C for 12 h. Finally, 4 g powder was compacted in cylindrical pellets using a uniaxial hydraulic press in a 12 mm (diameter) stainless die under 150 MPa. To minimize the sodium volatilization at high temperatures, the pressed pellet was buried in sacrificial powder of the same composition in a platinum crucible and calcined at various temperatures (850 to 1000 °C for 12 h) in a muffle

furnace. Upon cooling to 150 °C, these samples were transferred into an Argon atmosphere glovebox (MBraun; O<sub>2</sub> and H<sub>2</sub>O levels < 0.1 ppm). NMA111 sample calcined at 850 °C in pelletized form is labelled as 'Pellet-850', and the covering sacrificial powder sample is labelled as 'Powder-850'. NMA111 powder calcined at 1000 °C is labelled as 'Powder-1000'.

#### 2.2 Characterizations

To confirm the phase formation, powder x-ray diffraction (XRD) was performed on pellets and sacrificial powder samples heated at various temperatures using an Empyrean diffractometer from Malvern Panalytical (Cu- $K_\alpha$  radiation wavelength  $\lambda \approx 1.54$  Å). The *TOPAS academic* software was used to perform the Rietveld refinement of powder XRD data. The morphology and elemental mappings of the synthesized powders were studied using a scanning electron microscope (FESEM model JEOL-7610). The applied voltage was 15 kV, and images were captured at about 17000X magnification and a working distance of ~9 mm. For selected area electron diffraction (SAED) patterns and transmission electron microscopy (TEM) imaging, a JEOL-2100 microscope was used. A Thermofisher Scientific Naxsa instrument with a 1486.6 eV Al- $K_\alpha$  x-ray source was employed to record the x-ray photoelectron spectra (XPS). The elemental compositions of NMA111 pellet and powder samples were determined using an Agilent 5800 inductively coupled plasma optical emission spectrometer (ICP-OES).

For the electrochemical measurements, half-cells in CR2032 configuration employing the NMA111 cathodes (Powder-850 and Pellet-850) were assembled using sodium metal as the anode, glass fiber (Whatman G/D) as the separator, and 1M NaClO<sub>4</sub> in a 1:1 solution of EC:PC (ethylene carbonate and polypropylene carbonate) as the electrolyte. The cathode slurries were prepared using the NMA111 powder, PVDF (Polyvinylidene fluoride) as the binder, and Ketjen Black as the conducting carbon in the ratio 75:15:10. N-methyl-2-pyrrolidone was used as the solvent for the slurry, which was stirred for 10 h and then coated on aluminum foil using an automatic film coater. After drying in a vacuum oven overnight, the coated cathode was punched into 14 mm diameter discs. The mass loading for the active material was ~3 mg cm<sup>-2</sup>. A Neware battery tester (model CT-4008) was used for the GITT (galvanostatic intermittent titration technique) and galvanostatic charge-discharge (GCD) behaviors at various C-rates (1C current was taken 130 mA g<sup>-1</sup>). The impedance data for the NMA111 pellet and half-cell employing NMA111 as the cathode were collected using the Biologic electrochemical workstation (model: SP-50e) in the 10 mHz to 100 kHz frequency range. The same electrochemical workstation was also used for cyclic voltammetry (CV) and

chronoamperometry studies. Conductive silver paint was used as the ion-blocking electrodes on either side of the polished pellet for the impedance and chronoamperometry measurements.

#### 3 Results

#### 3.1 Crystal structure

The sintered pellets were ground using a pestle and mortar for powder XRD studies. The room temperature XRD patterns of the NMA111 pellet and sacrificial powder calcined at 850 °C for 12 h in the  $2\theta$  range of  $10^{\circ}$  to  $70^{\circ}$  are shown in Fig. 1. While all major peaks in the XRD pattern of the NMA111 pellet heated at 850 °C (labelled Pellet-850) match with those of the O3 phase reported in the literature, the XRD pattern of the NMA111 powder sample (Powder-850) is drastically different. Along with the O3 phase, peaks belonging to the P2 phase are clearly visible. Minor impurity peaks (at ~20° and 30°) belonging to the typical  $\beta$ -phase of layered oxides are also observed in both samples [41]. Such a variation in the phase structure of powder and pellet samples confirms the role that Na volatilization plays in the P2 and O3 phase formation. Volatilization of Na from the sodium transition metal layered oxide increases the oxygen-ion repulsion in the Na-O2 layers and pushes the adoption of prismatic coordination of the Na-sites [42].

The XRD pattern of the NMA111 powder heated at 1000 °C shows no peak corresponding to the O3 phase. This contrasts with other reports where the O3 phase formation is dominant at higher temperatures in Na<sub>0.8</sub>Mg<sub>0.06</sub>Ni<sub>0.34</sub>Mn<sub>0.54</sub>Ti<sub>0.06</sub>O<sub>2</sub> prepared by the solid-state reaction method using Na<sub>2</sub>CO<sub>3</sub> [43]. Recently, it has been shown by Mariappan et al. that suppression of the Na-volatilization during calcination at higher temperatures is crucial for the formation of a pure O3 phase [44]. The amounts of constituent elements in NMA111 Pellet-850 and Powder-850 samples, estimated using the inductively coupled plasma optical emission spectrometer, are provided in Table S2. The calculated amounts of various elements confirm higher Na volatilization in the sacrificial powder (0.18 Na loss in Powder-850 sample) than in the buried pellet (0.05 Na loss in Pellet-850). This corroborates the XRD results, where a significant amount of P2 phase is observed in the XRD pattern of the Powder-850 sample.

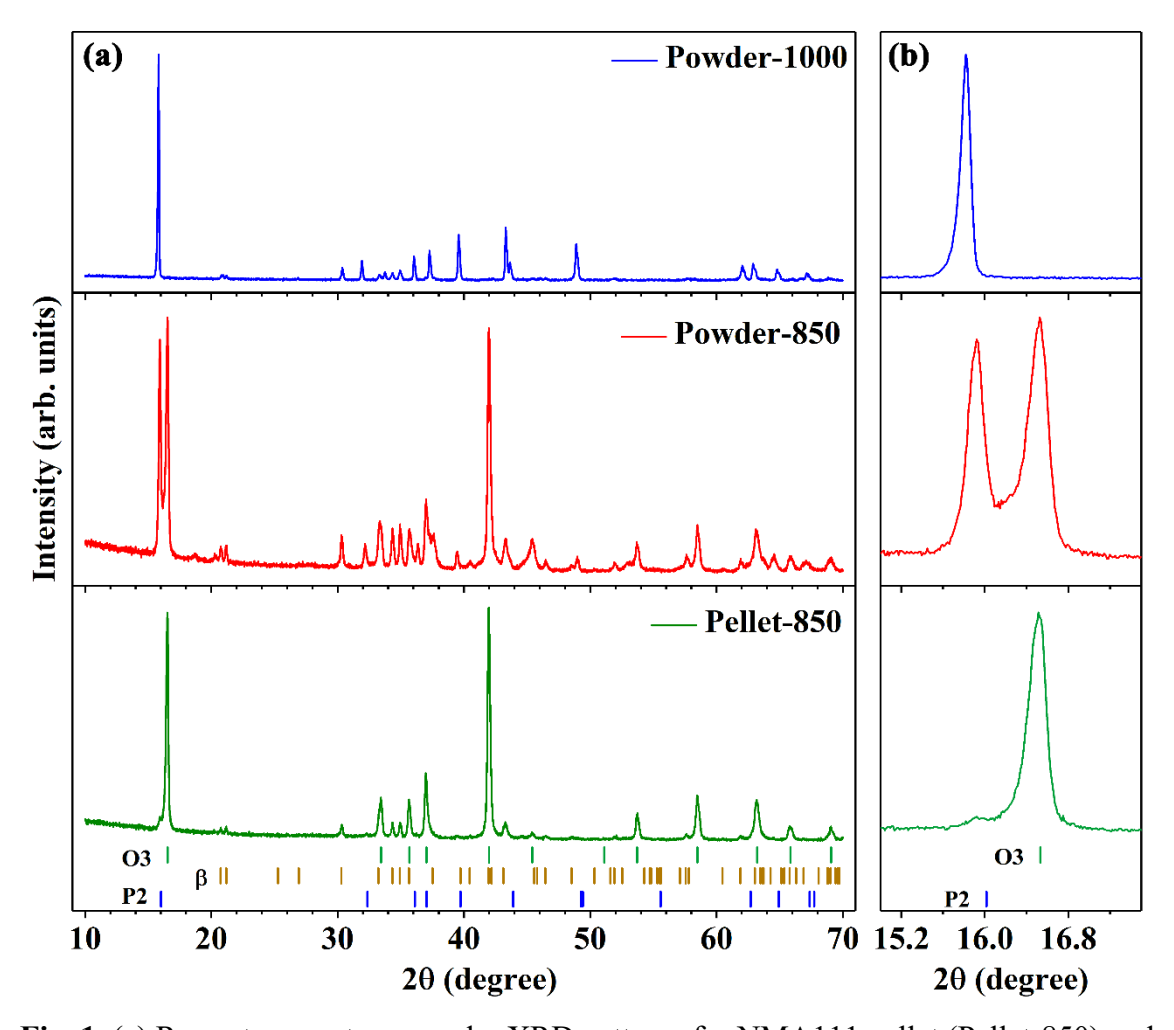


**Fig. 1.** (a) Room temperature powder XRD patterns for NMA111 pellet (Pellet-850) and sacrificial powder calcined at 850 °C (Powder-850), along with the powder heated at 1000 °C (Powder-1000). (b) The magnified view of patterns in the 15-17° range demonstrates the presence of P2 and O3 phases in the sacrificial powder.

To further analyze the NMA111 crystal structure, XRD data of the pelletized sample heated at 850 °C (Pellet-850) was refined based on the Rietveld method using the *TOPAS academic* software (Fig. 2). A combination of the O3-type ( $R\bar{3}m$ ), P2-type ( $P6_3/mmc$ ), and orthorhombic  $\beta$ -type ( $Pn2_1a$ ) structures was used for fitting, and the results are shown in Table S1. The refined pattern showed an excellent agreement with the experimental pattern. The lattice parameters obtained from the refinement are given in Table 1. The O3 phase proportion in this sample is ~87.8% with a minor (~3.5%) P2-type phase, and the rest 8.7% is  $\beta$  phase. For O3-type materials, the M-O2 interlayer spacing ( $S_{O-M-O}$ ) and Na-O2 interlayer spacing ( $S_{O-Na-O}$ ) are given by the following equations:

$$S_{0-M-0} = 2c \left(\frac{1}{3} - O_{\rm Z}\right) \tag{1}$$

$$S_{\text{O-Na-O}} = \frac{c}{3} - S_{\text{O-M-O}} \tag{2}$$

where c is the lattice parameter of the O3-type unit cell and  $O_z$  is the fractional coordinate of the oxygen ion along the z-axis. The calculated values of  $S_{\text{O-Na-O}}$  and  $S_{\text{O-M-O}}$  in NMA111 O3 phase were 3.170 Å and 2.185 Å. A schematic of the O3-crystal structure of NMA111 is shown in Fig. S1.

The Rietveld refinement profiles of the Powder-850 and Powder-1000 samples are shown in Fig. S2 and S3, respectively. The calculated lattice parameters, phase fractions, and other structural information are provided in Tables S3-S6. The P2 phase fraction in the sacrificial powder is 32% along with 6.1% NiO and 6.9%  $\beta$ -type phases. Further, the lattice parameter c of the O3 phase increases from 16.066 Å for the Pellet-850 sample to 16.085 Å for the Powder-850 sample.

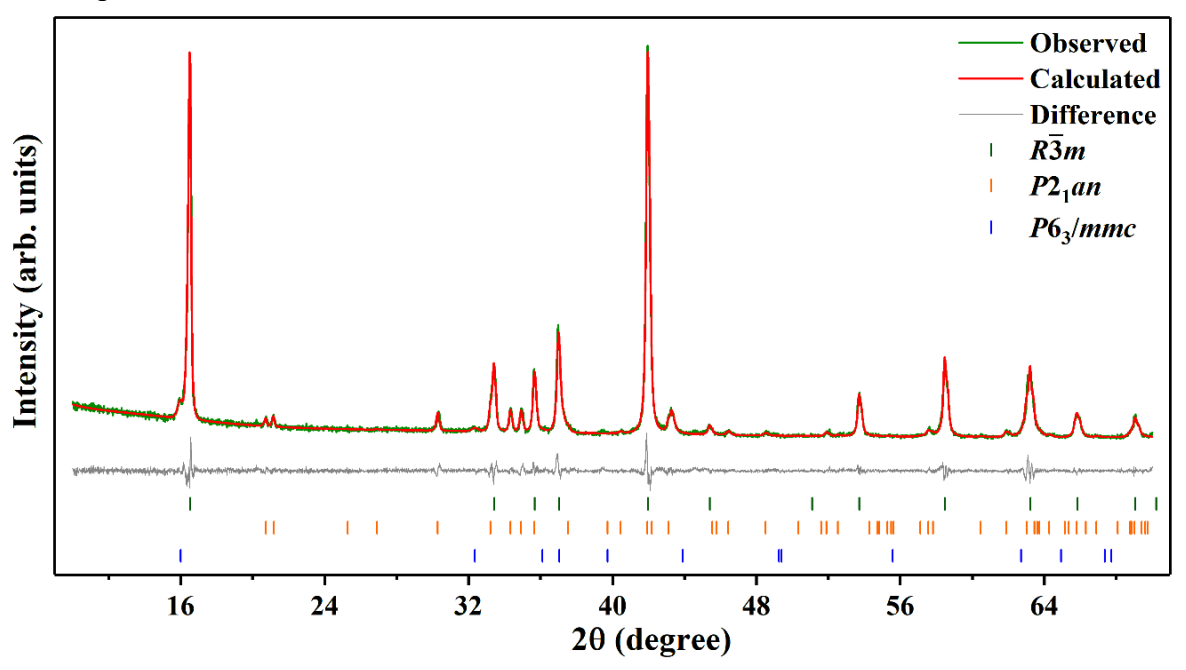


Fig. 2. Rietveld refinement profile for the NMA111 sample (Pellet-850).

A similar increase in the c of the P2 phase from 11.020 Å (Pellet-850) to 11.114 Å (Powder-850) is also noticeable (Table S3). This difference in the value of c for the Pellet-850 and Powder-850 is consistent with the ICP-OES data, confirming the different Na contents in these samples. A decrease in Na<sup>+</sup> content in Na-O2 layers weakens the shielding effect, causing an increase in  $O^{2-}$  O<sup>2-</sup> repulsion and increasing the lattice parameter c. A similar impact of increased Na volatilization in the Powder-1000 sample on the c is observed, where its value increases further to 11.2160 Å (Table S5). The NMA111 Powder-1000 sample also contains higher fractions of  $\beta$  (11%) and NiO (19%) phases.

**Table 1**: Refined structural parameters for NaMn<sub>1/3</sub>Al<sub>1/3</sub>Ni<sub>1/3</sub>O<sub>2</sub> pellet calcined at 850 °C.

Sample	O3 phase	P2 phase	β phase
Crystal system	Rhombohedral	Hexagonal	Orthorhombic
Space group	R3m	P6 <sub>3</sub> /mmc	$Pn2_1a$
Phase fractions	87.8%	3.5%	8.7%
Cell Parameters, Å			
	a = 2.9402(2)	a = 2.896(1)	a = 5.3852(7)
	b = 2.9402(2)	b = 2.896(1)	b = 5.2165(4)
	c = 16.066(6)	c = 11.020(8)	c = 7.032(9)
Cell Volume V, Å <sup>3</sup>	120.278(4)	80.06(6)	197.54(4)
Z	3	2	4
Phase density (g/cm <sup>3</sup> )	~4.219	~4.224	~3.42
Z	c = 16.066(6) $120.278(4)$ 3	c = 11.020(8) $80.06(6)$ 2	c = 7.032(9) $197.54(4)$ $4$

## 3.2 X-ray photoelectron spectroscopy

Fig. 3(a) depicts the X-ray photoelectron spectra of Na 1s, Ni 2p, Mn 2p, Al 2p, and O 1s for the NMA111 sample to ascertain the oxidation states of constituent elements. Two characteristic peaks at binding energies of  $\sim$ 854.9 eV (Ni 2p<sub>3/2</sub>) and  $\sim$ 872.5 eV (Ni 2p<sub>1/2</sub>), along with two much broader satellite peaks ( $\sim$ 860.8 & 879.4 eV), are visible in the Ni 2p spectra (Fig. 3a). The Ni 2p spectra confirm the 2+ oxidation state of Ni in the NMA111 sample. The Mn 2p spectrum has two prominent peaks at  $\sim$ 641.1 and  $\sim$ 652.8 eV, which are attributed to the Mn 2p<sub>3/2</sub> and Mn 2p<sub>1/2</sub> doublet, suggesting that Mn is in a 4+ oxidation state. Another broad peak at  $\sim$ 644.5 eV observed in Mn 2p has been attributed to being a satellite peak [45, 46] or due to the unresolved multiplet splitting [47].

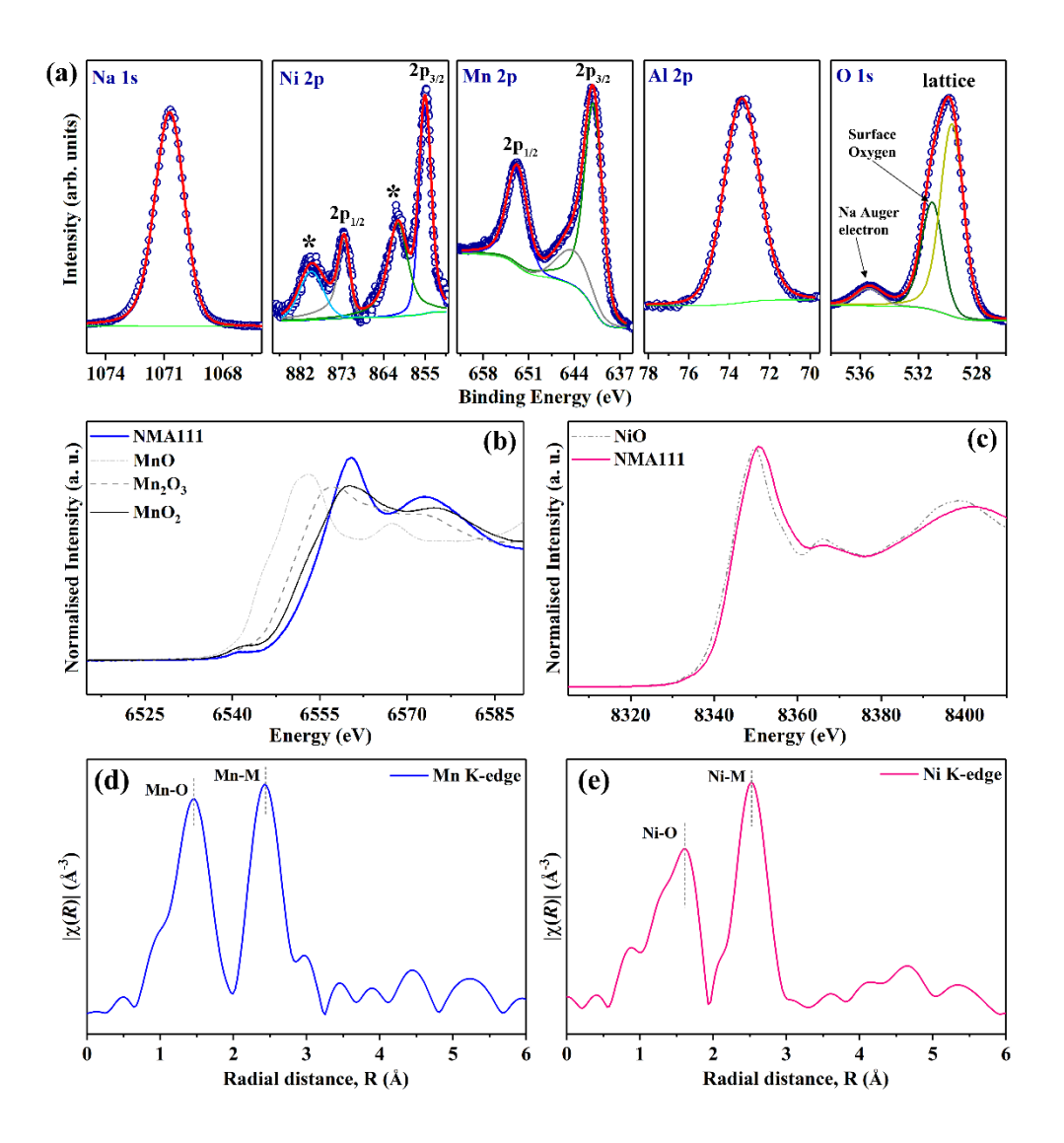


**Fig. 3**. (a) Fitted XPS data for NMA111 sample. XANES spectra at the b) Mn K-edge and c) Ni K-edge of the pristine NMA111 sample. EXAFS spectra at the (d) Mn K-edge and (d) Ni K-edge for the NMA111 powder.

Na 1s (at  $\sim$ 1070.7 eV) and Al 2p (at  $\sim$ 73.4 eV) peaks are consistent with the presence of Na<sup>+</sup> and Al<sup>3+</sup> in oxide materials. The O 1s spectrum shown in Fig. 3a has three peaks at  $\sim$ 529.7 eV,  $\sim$ 531.0 eV, and  $\sim$ 535.4 eV. The peak at 529.7 eV corresponds to lattice oxygen, whereas the other two peaks are attributed to the surface oxygen and Na Auger peak [48-50].

## 3.3 X-ray absorption spectroscopy

To further confirm the oxidation states and coordination structures of the NMA111 sample, synchrotron x-ray absorption spectroscopy was employed, and the resulting x-ray absorption near-edge structure (XANES) spectra at Mn and Ni K-edges are illustrated in Figs. 3b and 3c. The absorption edge energies of Mn and Ni K-edges are in similar ranges to those of standard

MnO<sub>2</sub> and NiO. The slight variations in the edge energies are due to the obvious differences in the crystal structures of NMA111 and MnO<sub>2</sub> & NiO. The XPS and XANES results confirm that the valencies of Mn and Ni atoms in NMA111 are +4 (for Mn) and +2 (for Ni). The extended x-ray absorption fine-structure (EXAFS) plots at Mn and Ni K-edges are given in Figs. 3d and 3e, respectively. The spectrum reveals that the scattering peak in the Mn K-edge spectrum at ~1.46 Å results from Mn–O interaction, and the peak at ~2.44 Å corresponds to the Mn–M (M: next-nearest metal ions). In the Ni K-edge spectrum, the peaks correspond to the scattering from the nearest oxygen anions (Ni–O) and the next-nearest metal ions (Ni–M) are at slightly larger distances at ~1.61 Å and ~2.53 Å, respectively.

#### 3.4 Microstructure

The morphology of as-prepared NMA111 samples was characterized by scanning electron microscopy and transmission electron microscopy. Fig. 4a shows the SEM image of the NMA111 Pellet-850 sample and agglomerated irregularly shaped particles with an average particle size of  $\sim 0.86 \pm 0.26~\mu m$ . Elemental mappings recorded using the energy dispersive X-ray spectroscopy (Fig. 4b1-b5) confirm the uniform distribution of the Na, Mn, Ni, and Al in the powder sample, and no segregation is apparent in NMA111. This suggests that the  $\beta$ -phase has a chemical composition similar to the major O3 phase. The SEM image of the Powder-850 sample, given in Fig. S4, shows a morphology similar to the Pellet-850 sample, suggesting that any differences in the electrochemical performance between these samples are driven by the phase structure. The high-resolution TEM (HRTEM) image (Fig. 4e shows the regular lattice fringe with a spacing of 2.55 Å, which matches well with the {100} planes of O3 NMA111. The bright spots seen in the selected area electron diffraction (SAED) recorded along the [331] zone axis are indexed to the representative reflections based on the O3 layered structure (Fig. 4d).

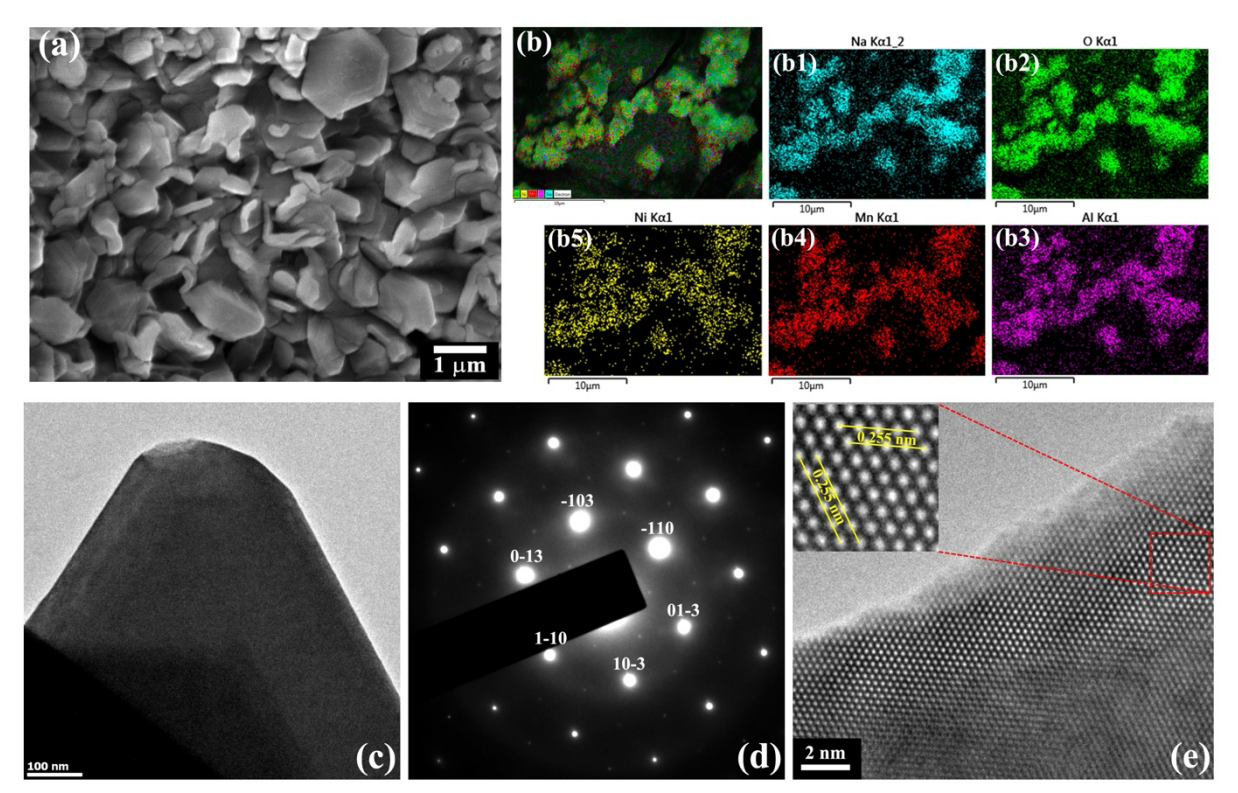


**Fig. 4.** SEM images of (a) NMA111 (Pellet-850) and (b) secondary electron (SE) image and EDS elemental mappings of (b1) Na, (b2) O, (b3) Al, (b4) Mn, and (b5) Ni in the NMA111. Bright-field TEM image (c), SAED pattern recorded along the [331] zone axis (d), and HRTEM images of the NMA111 sample along [001] axis (e).

#### 3.5. Electrical properties

To study the transport behavior of NMA111, impedance measurements were performed on the pelletized sample, and the room temperature Nyquist plot (-Z" versus Z'), along with the equivalent circuit fitting profile, is plotted in Fig. 5a. The equivalent circuit used to model the impedance data is shown as the inset. The two fitted semicircular arcs in higher and intermediate frequency regions correspond to the grain and grain boundary contributions to the overall impedance in the material. An inclined straight line feature at lower frequencies in the Nyquist plot confirmed the substantial Na-ion conduction in NMA111. The conductivity values were calculated using the fitted values of  $R_G & R_{GB}$  and the sample dimensions, and the values of the grain and grain boundary conductivities are ~2.59 × 10<sup>-6</sup> S cm<sup>-1</sup> and ~3.41 × 10<sup>-6</sup> S cm<sup>-1</sup>, respectively. It is important to mention that the NMA111 pellet used in this test (sintered at 850 °C) had a relative density (measured using the pellet's weight and dimensions) of only ~55%. Accordingly, the bulk (within-grain) conductivity value was corrected to account for the porosity using the Bruggeman model as given by Eq. 3,

$$\sigma^m = \sigma^0 \left( 1 - \frac{3}{2} p \right) \tag{3}$$

where  $\sigma^m$  is the measured conductivity of the sample from the impedance data,  $\sigma^0$  is the conductivity of the NMA111 sample with 0% porosity, and p = 0.45 is the fraction of the pores.

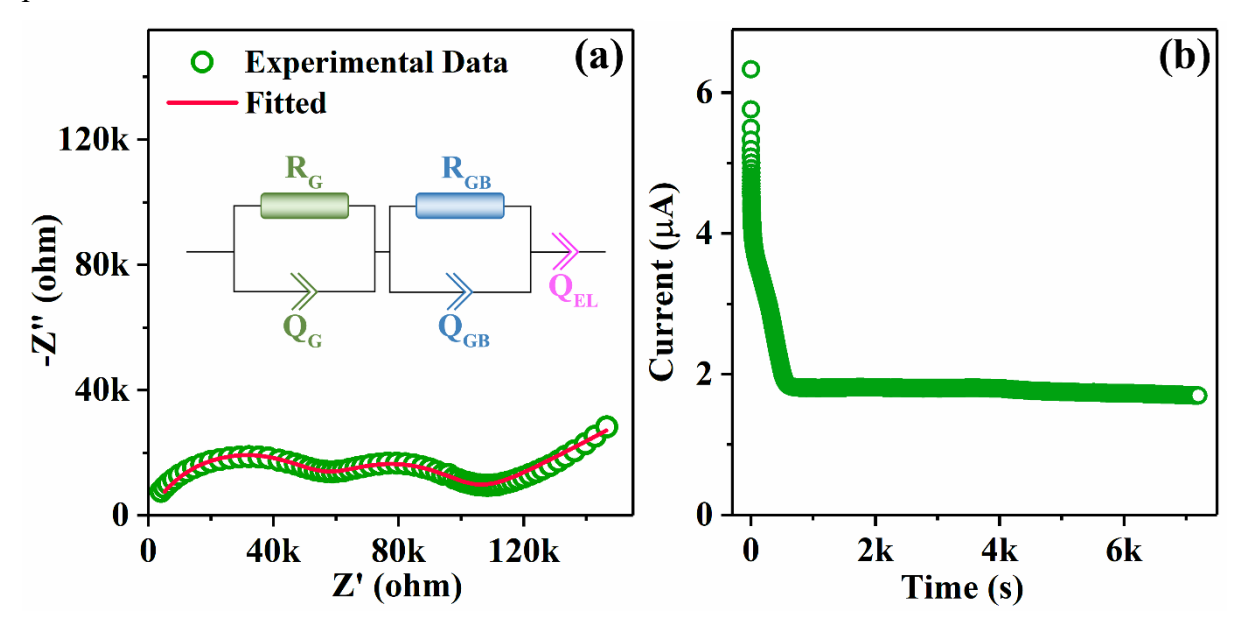


**Fig. 5.** (a) Nyquist plot of NMA111 pellet at room temperature (25 °C). The data was fitted using the equivalent circuit shown as the inset. (b) Chronoamperometry curve under 100 mV.

The corrected value of the grain conductivity at room temperature is ~  $7.97 \times 10^{-6}$  S cm<sup>-1</sup>. For cathode materials, both electronic and ionic conductivities are crucial in determining the rate performance of the cathode. To evaluate the contributions of Na-ions and electrons to the total conductivity, a polarization study under an applied DC voltage of 100 mV was conducted. The current value decreased from ~6.3  $\mu$ A at the start of the experiment (I<sub>0</sub>) to ~1.7  $\mu$ A once the steady-state (I<sub>e</sub>) is achieved, indicating a Na-ion transference number of about 0.73 (Fig. 5b). Thus, the values of room temperature bulk sodium-ion ( $\sigma_{N\alpha+}$ ) and electronic ( $\sigma_{e-}$ ) conductivities for the NMA are estimated to be ~5.82 × 10<sup>-6</sup> S cm<sup>-1</sup> and ~ 2.15 × 10<sup>-6</sup> S cm<sup>-1</sup>, respectively. The ionic conductivity of NMA111 is close to the values reported for other layered oxides such as Na[Li<sub>0.05</sub>(Ni<sub>0.25</sub>Fe<sub>0.25</sub>Mn<sub>0.5</sub>)<sub>0.95</sub>]O<sub>2</sub>, Na<sub>0.67</sub>Mn<sub>0.55</sub>Ni<sub>0.25</sub>Ti<sub>0.2-x</sub>Li<sub>x</sub>O<sub>2</sub>, etc. [51, 52].

## 3.4 Cyclic voltammetry

Cyclic voltammetry (CV) measurements were done on the NMA111 cathode in a half-cell configuration in the 1.5-4.0 V range. Fig. 6a shows the CV plots of the first two cycles at a scan rate of 0.1 mV s<sup>-1</sup>.

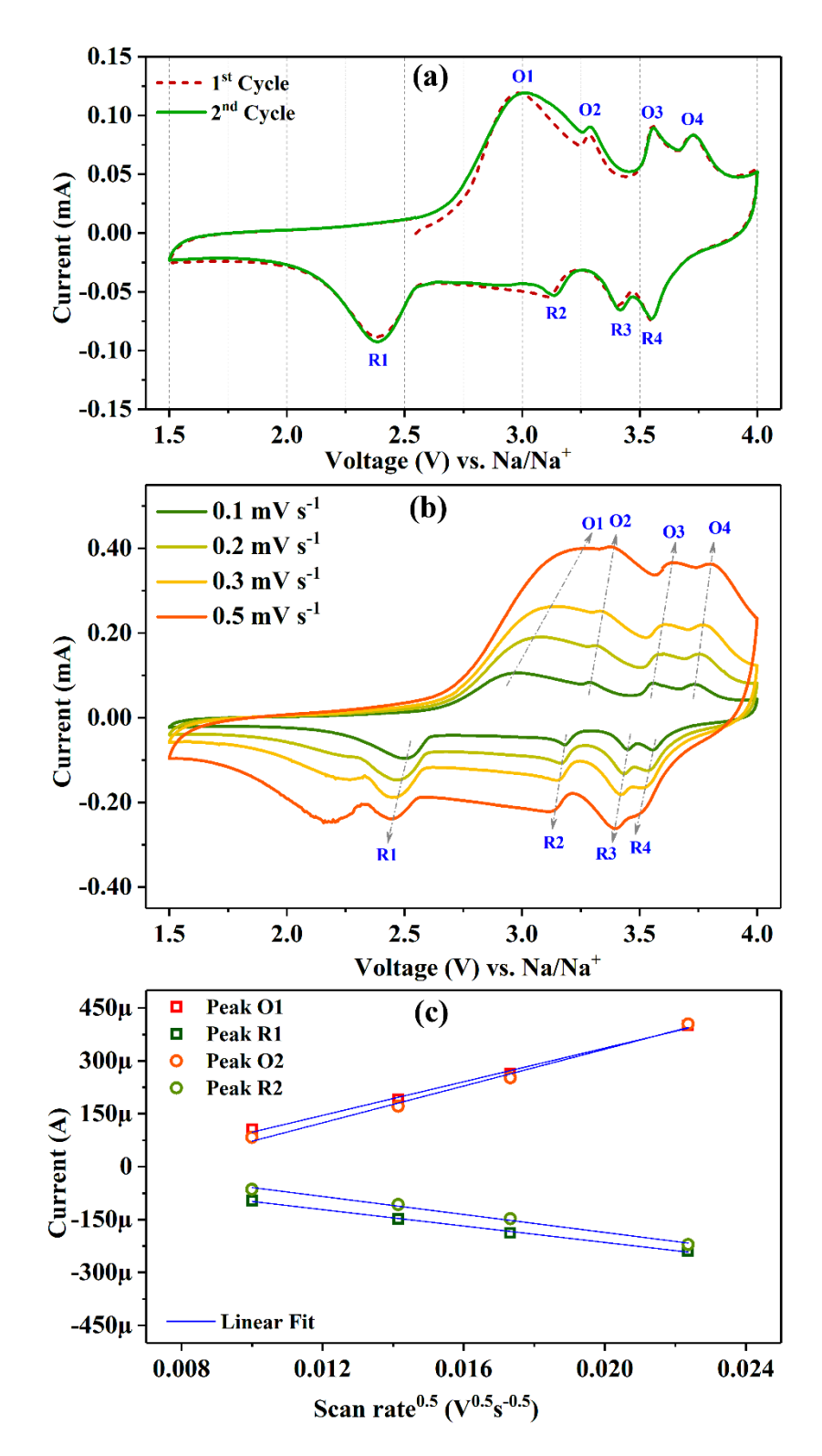


**Fig. 6.** Cyclic voltammograms of NMA111 within the voltage range of 1.5–4.0 V (a) first 2 cycles at 0.1 mV s<sup>-1</sup> and (b) at various scan rates from 0.1 to 0.5 mV s<sup>-1</sup>. (c) Linear relationship of peak currents with the square root of scan rate for oxidation (O1, O2), and reduction (R1, R2) peaks.

Four redox peaks are observed at ~3.01/2.39 V, ~3.29/3.14 V, ~3.56/3.41 V, and ~3.72/3.55 V in Fig. 6a. These four features are attributed to the Ni<sup>2+/3+</sup> redox activity, as reported in the literature. An additional peak at ~2.2 V during the reduction scan is observed for the scan rate 0.5 mV s<sup>-1</sup>. Interestingly, out of the four peaks, the O1/R1 redox peaks showed the largest polarization, indicating sluggish kinetics for this redox process. CV plots for NMA111 at various scan rates from 0.1 to 0.5 mV s<sup>-1</sup> are shown in Fig. 6b, and the peak currents ( $i_p$ ) increase with the increase in the scan rate. Further, there is a shift in the oxidation peaks to higher voltages with increasing scan rate. Randles–Ševčík equation (Eq. 4) is often used to estimate the Na-ion diffusion ( $D_{Na+}$ ) coefficients using the peak current versus the square root of scan rate ( $v^{0.5}$ ) of the cyclic voltammograms at various scan rates.

$$i_p = 2.69 \times 10^5 n^{3/2} SC \sqrt{D_{Na+} \nu} \tag{4}$$

Here, n, S, and C represent the number of electrons transferred in the redox process, the electrode area (cm²), and the concentration of Na (mol/cm³) in the electrode, respectively. The linear fittings of the  $i_p$  versus  $v^{0.5}$  for peaks O1/R1 and O2/R2 are shown in Fig. 6c, whereas those for O3/R3 and O4/R4 are provided in Fig. S5. A good linear relationship for all peaks suggests diffusion-controlled Na<sup>+</sup> extraction and insertion behaviour in NMA111 [53-55]. The calculated values of the diffusion coefficient for all four oxidation peaks for NMA111 are similar (in ~1.3 × 10<sup>-11</sup> cm² s<sup>-1</sup> to  $1.0 \times 10^{-11}$  cm² s<sup>-1</sup> range), while those for reduction peaks are slightly lower, with values lying in the  $4.3 \times 10^{-12}$  cm² s<sup>-1</sup> to  $2.5 \times 10^{-12}$  cm² s<sup>-1</sup> range.

#### 3.5 Electrochemical Behaviour

The electrochemical properties of the NMA111 sample were investigated in Na-half cells cycled at 0.1C (1C = 130 mAh g<sup>-1</sup>) in two different voltage windows, 2.0–4.0 V and 1.5–4.2 V. The first galvanostatic charge–discharge (GCD) curves of NMA111 in both voltage windows are shown in Fig. 7a. With the upper cut-off voltage of 4.0 V, the NMA111 shows a charging specific capacity of ~97 mAh g<sup>-1</sup>. Upon discharging to 2.0 V, the observed reversible capacity is ~87 mAh g<sup>-1</sup> (average voltage of 2.92 V), which corresponds to the insertion of 0.33 Na-ions per formula unit from the Ni<sup>2+</sup>/Ni<sup>3+</sup> redox process. The low Columbic efficiency (~89%) in the first cycle could be due to the electrolyte decomposition, formation of electrode-electrolyte interphase layers, etc. [56-58]. On charging the cell to 4.2 V, the specific capacity improved to ~129 mAh g<sup>-1</sup>; however, only a capacity of ~96 mAh g<sup>-1</sup> is reversible when discharged to 1.5 V in the first cycle. The first two GCD cycles of NMA111 cell discharged at

0.1C in 2.0-4.2 V are given in Fig. S6 and confirm only a partial reversibility of the capacity plateau above 4.0 V. Due to the poor Coulombic efficiency of the NMA cell when charged to 4.2 V, the upper cut-off voltage for the rate performance and the cyclability studies was limited to 4.0 V. The irreversible capacity loss above 4.0 V is attributed to the irreversible anionic redox and associated phase transitions reported in various Mn/Ni-based layered oxides [59-62]. The discharge profile of NMA111 (Fig. 7) does not show prominent plateaus above 2.5 V, which are seen in GCD profiles of NaMn<sub>0.5</sub>Ni<sub>0.5</sub>O<sub>2</sub> and Na<sub>0.67</sub>Mn<sub>0.67</sub>Ni<sub>0.33</sub>O<sub>2</sub> [60, 63-65]. This sloping-curve type profile is indicative of disorder induced by the Al<sup>3+</sup> in NMA111.

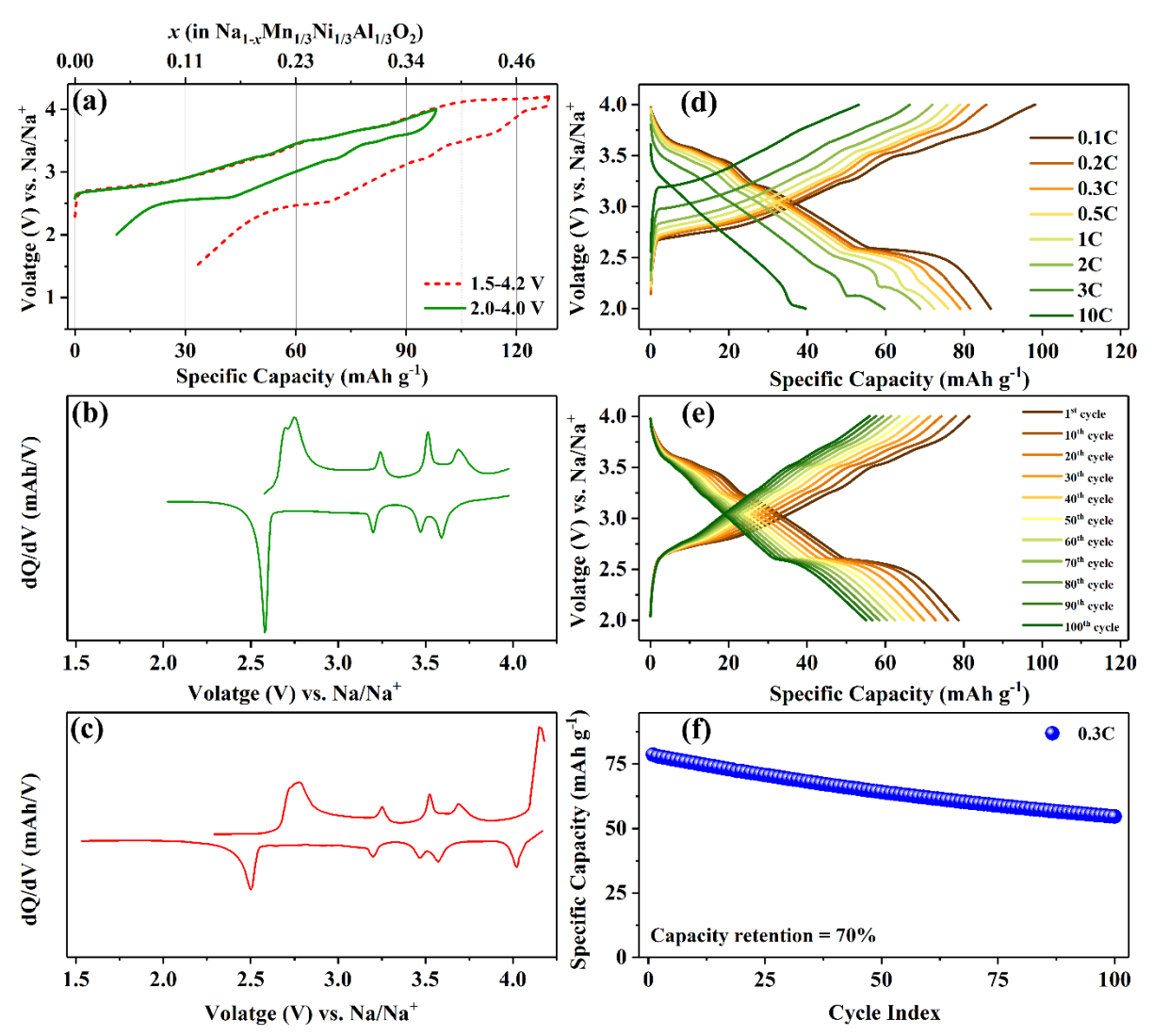


**Fig. 7.** GCD behaviour of NMA111: (a) first cycle GCD curves of NMA111 in 2.0-4.0 V and 1.5-4.2 V ranges. Corresponding dQ/dV vs. V plots (b) 2.0-4.0 V range and (c) 1.5-4.2 V range. (d) Rate performance, (e) GCD curves for selected cycles at 0.3C, and (f) cyclability.

The differential capacity (dQ/dV) vs. voltage (V) curves in Fig. 7b,c display four redox peaks in the 2.0–4.0 V range, whereas an additional redox peak appears when the cell is charged to 4.2 V. This peak in the dQ/dV vs. V plot and the corresponding plateau in Fig. 7a are attributed to the anionic redox process that has been reported in many Mn/Ni-based layered oxides. This redox process seems to be only partially reversible. The peaks in the 2.0-4.0 V range are attributed to Ni redox activity during phase transitions and/or Na-ion/vacancy ordering. The rate performance of the NMA111 cathode at different currents cycled in the 2.0-4.0 V range is illustrated in Fig. 7d, and it shows a specific capacity of ~87, ~72, and ~40 mAh g<sup>-1</sup> at 0.1C, 1C, and 10C, respectively. The long-term cyclability of NMA11 (Pellet-850) at 0.3C is shown in Fig. 7f, and the voltage profiles of selected cycles are shown in Fig. 7e. The initial discharge capacity for this sample is ~79 mAh g<sup>-1</sup>, which reduces to 55 mAh g<sup>-1</sup> after 100 cycles, indicating a capacity retention of ~70%. Interestingly, the additional peak observed at ~2.2 V in the CV reduction curve recorded at 0.5 mV s<sup>-1</sup> is also reflected in the GCD data at higher Crates (0.5C and above) as a small plateau in the discharging curve at a similar voltage. As this anomaly is not observed at low C rates and is prominent only at higher current densities, it suggests that a larger Na-ion concentration gradient in the cell might be inducing either the side reactions or some phase transition in the NMA111 cathode. Additional studies are needed to probe the mechanism behind this anomalous plateau in the discharge curve at higher C rates.

The cyclability plot for the Pellet-850 cathode at 1C and 3C (Fig. S7) shows that the capacity retention at higher current is quite poor, with only ~22% capacity available after 100 charge-discharge cycles at 3C. The capacity retention after 100 cycles at 1C is ~67.1%. Higher charge-discharge currents are known to cause larger strain in the cathode material and may cause larger volume changes during phase transitions, particle cracking, and exfoliation of cathode particles from the current collector. This would explain the comparatively poorer cyclability of NMA111 at high C rates. The average discharge voltage at 0.3C decreases from 2.87 V during the first cycle to 2.72 V in the 100<sup>th</sup> cycle (Fig. S8); whereas, the average charge voltage increased from 3.15 V to 3.30 V after 100 cycles. Such capacity fading and increased polarization during cycling could be attributed to the particle cracking as a result of structural degradation, increased side reactions causing interphase growth, and Na<sup>+</sup> kinetic limitations [65, 66]. The GCD curves for the NMA111 cathode prepared using the sacrificial powder (Powder-850) at various C-rates are provided in Fig. S9, and the long-term cyclability at 0.3C is plotted in Fig. S10. This sample shows a lower specific capacity (~74.8 mAh g<sup>-1</sup> at 0.1C and 55.1 mAh g<sup>-1</sup> at 1C) as compared to the Pellet-850 sample. Similarly, the capacity retention for

the Powder-850 cathode is inferior (~57.8%) to that of the Pellet-850 cathode (70%) after 100 cycles at 0.3C. The reason behind the poor performance of the NMA111 cathode prepared from sacrificial powder could be due to the creation of oxygen vacancies or a partial change in Ni oxidation state from +2 to +3 for charge balancing as a consequence of Na loss during calcination. As the capacity in NMA111 is predominantly due to the Ni<sup>2+/3+</sup> redox, any increase in Ni<sup>3+</sup> concentration will decrease the capacity. Moreover, this sample has a higher fraction of undesired phases (Fig. S2 and Table S3), which would also cause poor electrochemical performance.

To confirm the charge compensation mechanism, ex-situ XPS measurements were performed on the NMA111 cathode (Pellet-850) samples charged to 4.0 V and discharged to 1.5 V. Fig. S11 shows the Mn 2p and Ni 2p spectra. The Mn 2p spectrum for both states of charge is similar to that of the pristine powder sample, suggesting that there is no change in the oxidation state of Mn during the charge-discharge process. Ni 2p spectrum for the sample charged to 4.0 V, on the other hand, showed a shift in the peak position as well as peak broadening as compared to the spectrum of the cathode discharged to 1.5 V. These results thus confirm that only Ni<sup>2+/3+</sup> redox activity is responsible for the capacity observed in the NMA111 sample when cycles between 1.5 V and 4.0 V.

## 3.6 GITT

To determine the value of the room temperature diffusion coefficient of Na-ions for the NMA111 sample, the galvanostatic intermittent titration technique (GITT) was carried out. Fig. 8 represents the resultant voltage profile and the diffusion coefficient ( $D_{Na+}$ ) values at different states of charge after the formation cycle. A constant current pulse of 13 mA g<sup>-1</sup> (0.1C) was applied for a duration of 10 minutes, then 30 minutes were given for the relaxation (no current applied), and the steps were repeated during the charge-discharge process (1.5-4.0 V). Equation 5 was used for the calculation of the  $D_{Na+}$ .

$$D_{Na^{+}} = \frac{4}{\pi \tau} \left(\frac{m_{B}}{\rho S}\right)^{2} \left(\frac{\Delta E_{S}}{\Delta E_{T}}\right)^{2} \qquad \left(t \ll \frac{L^{2}}{D}\right)$$
 (5)

Here,  $\Delta E_{\tau}$  and  $\Delta E_{S}$  correspond to the change in the voltage during the current pulse and the equilibrium value for the cathode. The molar density, surface area, mass loading for the active material, and duration of the constant pulse (10 minutes) are denoted by  $\rho$ , S,  $m_{B}$ , and  $\tau$ , respectively.

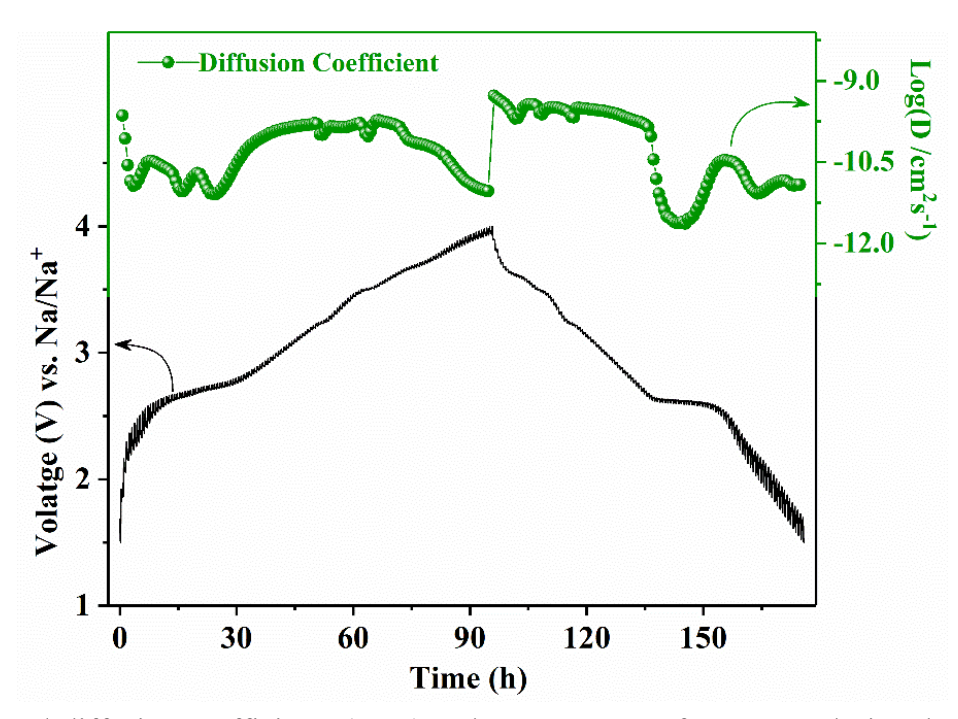


**Fig. 8.** Na $^+$  diffusion coefficients ( $D_{Na+}$ ) and GITT curves of NMA111 during the charge-discharge process at 0.1C.

NMA111 exhibits the diffusion coefficients in the range of  $5.29 \times 10^{-10}$  to  $8.80 \times 10^{-12}$  cm<sup>2</sup> s<sup>-1</sup>. During the charging process, comparatively lower values of  $D_{Na+}$  are observed when the cell voltage is below 2.7 V, and then gradually increase to higher values reaching  $1.85 \times 10^{-10}$  cm<sup>2</sup> s<sup>-1</sup> due to the faster Ni<sup>2+/3+</sup> redox kinetics in the 2.7-3.5 V range. The value of  $D_{Na+}$  starts decreasing when the cell is charged above 3.5 V, reaching a minimum value of  $9.47 \times 10^{-12}$  cm<sup>2</sup> s<sup>-1</sup> at 4.0 V. At the onset of discharging, the value of the diffusion coefficient reaches its maximum of  $5.29 \times 10^{-10}$  cm<sup>2</sup> s<sup>-1</sup>, decreases marginally till the cell voltage reaches 2.5 V, and then decreases significantly. These variations in the Na-ion diffusion coefficient could be due to the Ni-redox kinetics and the phase transformations during the charge-discharge process. Further,  $D_{Na+}$  values estimated from GITT and CV fitting are of a similar order.

## 3.7 Electrochemical impedance spectroscopy

In situ electrochemical impedance spectroscopy (EIS) measurements were performed to further explore the Na-ion kinetics in the NMA111 cathode. These measurements were carried out on the half-cell during charging after the formation cycle in the 100 kHz to 10 mHz frequency range. For the formation cycle, the cell was charged to 4.0 V and then discharged to 1.5 V at 0.1C. The cell was allowed to rest for 2 h to achieve the equilibrium OCV at each SOC before conducting the EIS measurement. The Nyquist plots of the NMA111 cell showed

overlapped semi-circular arcs in the high-frequency region and a straight line in the low-frequency region at all voltages (Fig. 9a). Usually, the impedance response of such cells has contributions from the electrolyte resistance, the interphase layers formed on electrode surfaces, the charge-transfer process, and the Na-ion diffusion in electrodes [67-69]. Deconvoluting these processes from the Nyquist plots using equivalent circuit modeling is often challenging due to their intertwined responses in the medium-high frequency region [70, 71].

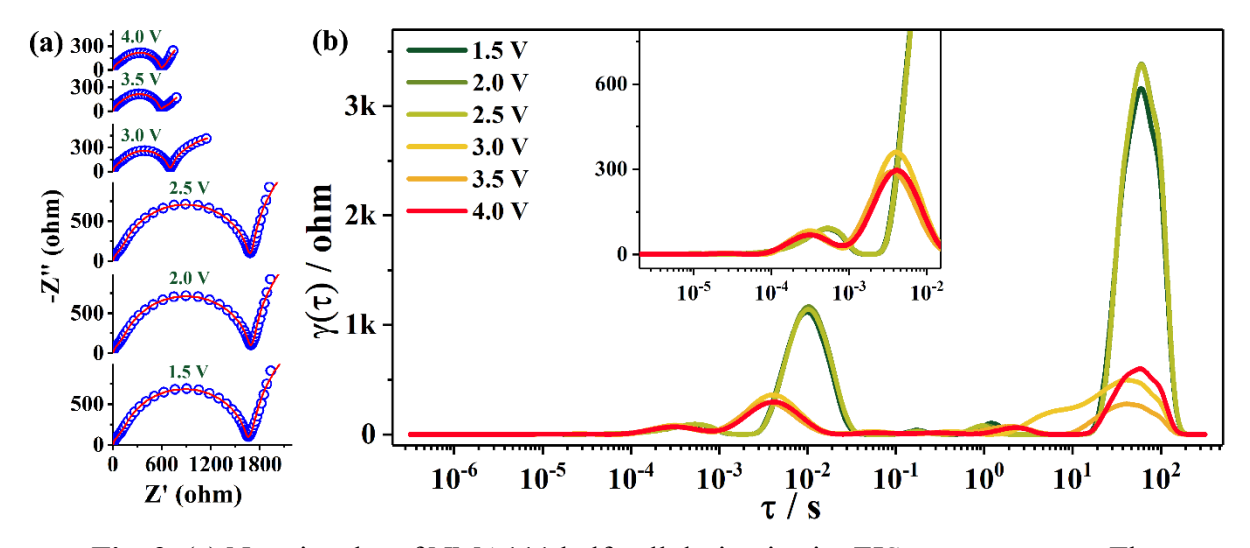


**Fig. 9.** (a) Nyquist plot of NMA111 half-cell during in situ EIS measurements. The corresponding DRT transformations are plotted in (b).

Accordingly, the distribution of relaxation time (DRT) technique was utilized to directly distinguish the timescale for these overlapping electrochemical processes, and the transformed response is shown in Fig. 9b [71, 72]. The peaks observed in this figure could be divided into the Na<sup>+</sup> transport across the cathode interphase layers (CEI, in the range  $10^{-4}$  to  $10^{-3}$  s), charge transfer resistance (in the  $10^{-3}$  to  $10^{-1}$  s range), and Na<sup>+</sup> diffusion (~ $10^{-1}$  to 100 s range) in the NMA111 particles [69, 73]. The impedance values associated with the processes are reflected by the relaxation-based function  $\gamma$  for corresponding peaks. The peak height corresponding to the CEI response remains almost constant, and only a marginal change in relaxation time ( $\tau$ ) is noticeable when the cell is charged to 3.0 V. This suggests a stable CEI formation in NMA111 at all voltages in the 1.5 to 4.0 V range. Similarly, the charge transfer and Na<sup>+</sup> diffusion response show minimal variation below 2.5 V. However, upon charging the cell to 3.0 V and above, the charge-transfer & Na<sup>+</sup> diffusion peaks decrease drastically (also noticeable from the Nyquist plots) and the corresponding  $\tau$  shifts to lower values, indicating faster Na<sup>+</sup> transport kinetics [73]. These results are consistent with the GCD behavior of

NMA111. There is almost no capacity exhibited by the NMA111 below 2.5 V during charging, and the  $Ni^{2+}$  to  $Ni^{3+}$  oxidation reaction stabilizes only above ~2.7 V (Fig. 7).

The SEM images of the NMA111 (Pellet-850) coated cathode harvested from the half-cell after 100 cycles at 0.3C are given in Fig. S12. While no clear cracks are visible in the SEM images of the post-cycled cathode particles, some amount of surface degradation is discernible. The in-situ EIS measurements (at 2.0 V, 3.0 V, and 4.0 V) were carried out for the NMA111 (Pellet-850) half-cell charged-discharged for 100 cycles at 0.3C to probe the changes in the contribution of various components to the overall impedance. The analysis of the equivalent circuit fitted EIS results indicates that the overall cell resistance increased after cycling at all three voltages, the semicircular arcs in the mid-frequency range in the Nyquist plot of cycled cathodes become distinct, and with the increase in the cell voltage, the overall resistance of the cycled cell decreases from ~2956  $\Omega$  at 2.0 V to ~902  $\Omega$  at 4.0 V (Fig. S13). The equivalent circuit used for fitting the impedance data is shown in Fig. S12, rightmost panel. Further, the overall cell resistance increases from ~1724  $\Omega$  to ~2956  $\Omega$  at 2.0 V, from ~715  $\Omega$  to 1535  $\Omega$ at 3.0 V, and from  $\sim 602~\Omega$  to 902  $\Omega$  at 4.0 V after 100 cycles. This increase in cell resistance is contributed to by both the increased interphase layers' resistance and the charge-transfer resistance. The increase in the resistance of the interphase layers formed on the electrodes' surfaces is typically caused by the detrimental electrolyte-electrode reactions [46, 74, 75]. Further, the volume changes caused by the phase transformations during the charge-discharge process induce structural deformations that could lead to particle cracking and exfoliation of the cathode particles from the current collector or conductive carbon matrix [76, 77]. These phenomena hamper the Na-ion diffusion and lead to increased cell resistance and capacity decay with cycling.

## **4 Conclusions**

In summary, an O3-type NaNi<sub>1/3</sub>Mn<sub>1/3</sub>Al<sub>1/3</sub>O<sub>2</sub> (NMA111) was prepared by calcining the powder at 850 °C via a sol-gel route. Minimizing the Na volatilization by covering the pelletized sample with sacrificial powder of the same composition was crucial in suppressing the formation of the P2-type phase, as confirmed by XRD analysis. The NMA111 cathode delivered an initial discharge capacity of ~87 mAh g<sup>-1</sup> at 0.1C in the 2.0 to 4.0 V range with an average voltage of ~2.92 V. Upon increasing the voltage to 4.2 V, the initial discharge specific capacity improved to ~96.6 mAh g<sup>-1</sup>, but the fading is severe. A mostly slanted voltage profile, albeit with a minor discharge plateau at ~2.5 V, suggested a solid-solution

type (de)intercalation mechanism in NMA111. The charge compensation is via the activation of the Ni<sup>2+/3+</sup> redox couple, as confirmed by the ex-situ XPS measurements showing Ni 2p shifts consistent with Ni<sup>2+/3+</sup> redox. This study demonstrates a practical route to stabilize O3-type layered cathodes for Na-ion batteries.

#### **CRediT** authorship contribution statement

Neha Dagar: Writing – review & editing, Writing – original draft, Methodology, Formal analysis, Data curation, Conceptualization. Samriddhi Saxena: Writing – review & editing. Sonia Deswal: Writing – review & editing, Data curation. Pradeep Kumar: Writing – review & editing, Data curation. Karthik Chinnathambi: Writing – review & editing, Data curation. Sunil Kumar: Writing – review & editing, Supervision, Project administration, Investigation, Funding acquisition, Formal analysis, Data curation, Conceptualization.

#### **Conflict of interest statement**

The authors declare no conflict of interest.

## Acknowledgments

This work was financially supported by the Ministry of Education, Government of India (grant number: MoE-STARS/STARS-2/2023-0365). ND acknowledges the UGC-JRF scheme of the Government of India (Grant no. 231610004459). This research utilized the Transmission Electron Microscope (TEM) in the Boise State University FaCT Core Facility, RRID: SCR\_024733, which receives support from the National Institutes of Health [NIH] under the Institutional Development Awards [IDeA] Program of the National Institute of General Medical Sciences [NIGMS] via grants P20GM148321 and P20GM103408.

## Data availability statement

The data supporting the findings of this study are available from the corresponding author upon reasonable request.

## References

- [1] M.D. Slater, D. Kim, E. Lee, C.S. Johnson, Sodium-Ion Batteries, Adv. Funct. Mater., 23 (2013) 947-958 <a href="https://doi.org/10.1002/adfm.201200691">https://doi.org/10.1002/adfm.201200691</a>.
- [2] J.Y. Hwang, S.T. Myung, Y.K. Sun, Sodium-ion batteries: Present and future, Chem. Soc. Rev., 46 (2017) 3529-3614 <a href="https://doi.org/10.1039/c6cs00776g">https://doi.org/10.1039/c6cs00776g</a>.

- [3] N. Yabuuchi, K. Kubota, M. Dahbi, S. Komaba, Research Development on Sodium-Ion Batteries, Chem. Rev., 114 (2014) 11636-11682 <a href="https://doi.org/10.1021/cr500192f">https://doi.org/10.1021/cr500192f</a>.
- [4] S. Wang, C. Sun, N. Wang, Q. Zhang, Ni- and/or Mn-based layered transition metal oxides as cathode materials for sodium ion batteries: status, challenges and countermeasures, J. Mater. Chem. A, 7 (2019) 10138-10158 http://dx.doi.org/10.1039/C8TA12441H.
- [5] M. Chen, Q. Liu, S.-W. Wang, E. Wang, X. Guo, S.-L. Chou, High-Abundance and Low-Cost Metal-Based Cathode Materials for Sodium-Ion Batteries: Problems, Progress, and Key Technologies, Adv. Energy Mater., 9 (2019) 1803609

  <a href="https://doi.org/10.1002/aenm.201803609">https://doi.org/10.1002/aenm.201803609</a>.
- [6] V. Palomares, P. Serras, I. Villaluenga, K. Hueso, J. Gonzalez, T. Rojo, Na-ion Batteries, Recent Advances and Present Challenges to Become low Cost Energy Storage Systems, Energy Environ. Sci., 5 (2012) 5884-5901 <a href="https://doi.org/10.1039/C2EE02781J">https://doi.org/10.1039/C2EE02781J</a>.
- [7] J. Cong, S.-h. Luo, P.-y. Li, X. Yan, L.-x. Qian, S.-x. Yan, Stable cycling performance of lituium-doping  $Na_{3-x}Li_xV_2(PO_4)_3/C$  ( $0 \le x \le 0.4$ ) cathode materials by Na-site manipulation strategy, Appl. Surf. Sci., 643 (2024) 158646 <a href="https://doi.org/10.1016/j.apsusc.2023.158646">https://doi.org/10.1016/j.apsusc.2023.158646</a>.
- [8] P. Li, T. Yuan, J. Qiu, H. Che, Q. Ma, Y. Pang, Z.-F. Ma, S. Zheng, A comprehensive review of layered transition metal oxide cathodes for sodium-ion batteries: The latest advancements and future perspectives, Mater. Sci. Eng. R Rep, 163 (2025) 100902 <a href="https://doi.org/10.1016/j.mser.2024.100902">https://doi.org/10.1016/j.mser.2024.100902</a>.
- [9] A. Sengupta, A. Kumar, G. Barik, A. Ahuja, J. Ghosh, H. Lohani, P. Kumari, T.K. Bhandakkar, S. Mitra, Lower Diffusion-Induced Stress in Nano-Crystallites of P2-Na<sub>2/3</sub>Ni<sub>1/3</sub>Mn<sub>1/2</sub>Ti<sub>1/6</sub>O<sub>2</sub> Novel Cathode for High Energy Na-ion Batteries, Small, 19 (2023) 2206248 <a href="https://doi.org/10.1002/smll.202206248">https://doi.org/10.1002/smll.202206248</a>.
- [10] N. Dagar, S. Saxena, H.N. Vasavan, A.K. Das, P. Gami, S. Deswal, P. Kumar, S. Kumar, Distinct electrochemical behavior of P3 and P2 polytypes of Mn/Ni-based Na-ion battery cathode, Mater. Lett., 369 (2024) 136768

  <a href="https://doi.org/10.1016/j.matlet.2024.136768">https://doi.org/10.1016/j.matlet.2024.136768</a>.
- [11] C. Zhao, Q. Wang, Z. Yao, J. Wang, B. Sánchez-Lengeling, F. Ding, X. Qi, Y. Lu, X. Bai, B. Li, H. Li, A. Aspuru-Guzik, X. Huang, C. Delmas, M. Wagemaker, L. Chen, Y.-S. Hu, Rational design of layered oxide materials for sodium-ion batteries, Science, 370 (2020) 708-711 <a href="https://doi.org/10.1126/science.aay9972">https://doi.org/10.1126/science.aay9972</a>.

- [12] C. Delmas, C. Fouassier, P. Hagenmuller, Structural classification and properties of the layered oxides, Physica B+C, 99 (1980) 81-85 <a href="https://doi.org/10.1016/0378-4363(80)90214-4">https://doi.org/10.1016/0378-4363(80)90214-4</a>.
- [13] C. Delmas, Sodium and Sodium-Ion Batteries: 50 Years of Research, Adv. Energy Mater., 8 (2018) 1703137 <a href="https://doi.org/10.1002/aenm.201703137">https://doi.org/10.1002/aenm.201703137</a>.
- [14] C. Shi, L. Wang, X.a. Chen, J. Li, S. Wang, J. Wang, H. Jin, Challenges of layer-structured cathodes for sodium-ion batteries, Nanoscale Horiz., 7 (2022) 338-351 <a href="https://doi.org/10.1039/D1NH00585E">https://doi.org/10.1039/D1NH00585E</a>.
- [15] S.-W. Kim, D.-H. Seo, X. Ma, G. Ceder, K. Kang, Electrode Materials for Rechargeable Sodium-Ion Batteries: Potential Alternatives to Current Lithium-Ion Batteries, Adv. Energy Mater., 2 (2012) 710-721 <a href="https://doi.org/10.1002/aenm.201200026">https://doi.org/10.1002/aenm.201200026</a>.
- [16] J. Feng, S.-h. Luo, L. Qian, S. Yan, Q. Wang, X. Ji, Y. Zhang, X. Liu, P. Hou, F. Teng, Properties of the "Z"-Phase in Mn-Rich P2-Na<sub>0.67</sub>Ni<sub>0.1</sub>Mn<sub>0.8</sub>Fe<sub>0.1</sub>O<sub>2</sub> as Sodium-Ion-Battery Cathodes, Small, 19 (2023) 2208005 <a href="https://doi.org/10.1002/smll.202208005">https://doi.org/10.1002/smll.202208005</a>.
- [17] H.N. Vasavan, M. Badole, S. Saxena, V. Srihari, A.K. Das, P. Gami, N. Dagar, S. Deswal, P. Kumar, H.K. Poswal, S. Kumar, Rational design of an optimal Al-substituted layered oxide cathode for Na-ion batteries, Electrochim. Acta, 494 (2024) 144457 <a href="https://doi.org/10.1016/j.electacta.2024.144457">https://doi.org/10.1016/j.electacta.2024.144457</a>.
- [18] H.N. Vasavan, M. Badole, S. Saxena, V. Srihari, A.K. Das, P. Gami, S. Deswal, P. Kumar, S. Kumar, Unveiling the potential of P3 phase in enhancing the electrochemical performance of a layered oxide cathode, Mater. Today Energy, 37 (2023) 101380 <a href="https://doi.org/10.1016/j.mtener.2023.101380">https://doi.org/10.1016/j.mtener.2023.101380</a>.
- [19] N. Dagar, S. Saxena, H.N. Vasavan, A.K. Das, P. Gami, S. Deswal, P. Kumar, K. Chinnathambi, V. Rathee, S. Kumar, Ti-Substitution Facilitating Anionic Redox and Cycle Stability in a P2-Type Na<sub>2/3</sub>Mn<sub>2/3</sub>Ni<sub>1/3</sub>O<sub>2</sub> Na-Ion Battery Cathode, Energy & Fuels, 39 (2025) 3348-3358 <a href="https://doi.org/10.1021/acs.energyfuels.4c05945">https://doi.org/10.1021/acs.energyfuels.4c05945</a>.
- [20] W.L. Pang, X.H. Zhang, J.Z. Guo, J.Y. Li, X. Yan, B.H. Hou, H.Y. Guan, X.L. Wu, P2-type Na<sub>2/3</sub>Mn<sub>1-x</sub>Al<sub>x</sub>O<sub>2</sub> cathode material for sodium-ion batteries: Al-doped enhanced electrochemical properties and studies on the electrode kinetics, J. Power Sources, 356 (2017) 80-88 https://doi.org/10.1016/j.jpowsour.2017.04.076.

- [21] K. Kubota, T. Asari, S. Komaba, Impact of Ti and Zn Dual-Substitution in P2 Type Na<sub>2/3</sub>Ni<sub>1/3</sub>Mn<sub>2/3</sub>O<sub>2</sub> on Ni–Mn and Na-Vacancy Ordering and Electrochemical Properties, Adv. Mater., 35 (2023) 2300714 <a href="https://doi.org/10.1002/adma.202300714">https://doi.org/10.1002/adma.202300714</a>.
- [22] T. Park, J. Jeong, S. Kang, J. Kim, K. Min, Revealing the role of dopants to suppress phase transition in biphasic layered transition metal oxide cathodes for sodium-ion batteries, J. Power Sources, 640 (2025) 236718 <a href="https://doi.org/10.1016/j.jpowsour.2025.236718">https://doi.org/10.1016/j.jpowsour.2025.236718</a>.
- [23] H.N. Vasavan, M. Badole, S. Dwivedi, D. Kumar, P. Kumar, S. Kumar, Enhanced rate performance and specific capacity in Ti-substituted P2-type layered oxide enabled by crystal structure and particle morphology modifications, Chem. Eng. J., 448 (2022) 137662 https://doi.org/10.1016/j.cej.2022.137662.
- [24] H.N. Vasavan, M. Badole, S. Dwivedi, S. Kumar, Structural and transport properties of P2-Type Na<sub>0.70</sub>Ni<sub>0.20</sub>Cu<sub>0.15</sub>Mn<sub>0.65</sub>O<sub>2</sub> layered oxide, Ceram. Int., 48 (2022) 28986-28993 <a href="https://doi.org/10.1016/j.ceramint.2022.04.206">https://doi.org/10.1016/j.ceramint.2022.04.206</a>.
- [25] J. Cabana, N.A. Chernova, J. Xiao, M. Roppolo, K.A. Aldi, M.S. Whittingham, C.P. Grey, Study of the Transition Metal Ordering in Layered  $Na_xNi_{x/2}Mn_{1-x/2}O_2$  (2/3  $\leq$  x  $\leq$  1) and Consequences of Na/Li Exchange, Inorg. Chem., 52 (2013) 8540-8550 https://doi.org/10.1021/ic400579w.
- [26] L.-L. Zhao, Y.-S. Zhao, J.-W. Yin, P.-F. Wang, Z.-L. Liu, Y.-R. Zhu, Y. Xie, J. Shu, T.-F. Yi, High-entropy strategy to reshape O3-type cathodes for sodium-ion batteries: From structural regulation to performance leap, J. Energy Storage, 132 (2025) 117894 <a href="https://doi.org/10.1016/j.est.2025.117894">https://doi.org/10.1016/j.est.2025.117894</a>.
- [27] F. Zhang, Z. Yang, B. He, Y. Xin, J. Zhang, W. Liu, S. Cai, H. Tian, Y. Yang, Tailoring Local Chemistry of O3-Type Ni/Fe/Mn-Based Layered Oxide Cathodes for High-Performance Sodium-Ion Batteries, ACS Nano, 19 (2025) 23011-23027 <a href="https://doi.org/10.1021/acsnano.5c02960">https://doi.org/10.1021/acsnano.5c02960</a>.
- [28] J. Wang, Y.-F. Zhu, Y. Su, J.-X. Guo, S. Chen, H.-K. Liu, S.-X. Dou, S.-L. Chou, Y. Xiao, Routes to high-performance layered oxide cathodes for sodium-ion batteries, Chem. Soc. Rev., 53 (2024) 4230-4301 <a href="https://doi.org/10.1039/D3CS00929G">https://doi.org/10.1039/D3CS00929G</a>.
- [29] A. Namazbay, M. Karlykan, L. Rakhymbay, Z. Bakenov, N. Voronina, S.-T. Myung, A. Konarov, Towards high-performance sodium-ion batteries: A comprehensive review on

- $Na_xNi_yFe_zMn_{1-(y+z)}O_2$  cathode materials, Energy Storage Mater., 77 (2025) 104212 https://doi.org/10.1016/j.ensm.2025.104212.
- [30] R. Huang, S. Luo, P. Li, Q. Sun, G. Hao, J. Feng, L. Qian, S. Yan, J. Guo, Properties of Rich-Nae Effect and Zero-Phase Transition in P2–Na<sub>0.67</sub>(Ni<sub>0.1</sub>Mn<sub>0.8</sub>Fe<sub>0.1</sub>)<sub>1–x</sub>Mg<sub>x</sub>O<sub>2</sub> Cathodes for Rapid and Stable Sodium Storage, ACS Sustain. Chem. Eng., 12 (2024) 16759-16769 <a href="https://doi.org/10.1021/acssuschemeng.4c07004">https://doi.org/10.1021/acssuschemeng.4c07004</a>.
- [31] R. Huang, S. Luo, Q. Sun, L. Qian, X. Liu, S. Yan, P2/O3 biphasic Fe/Mn based cathodes for simultaneously realizing kinetic-enhancement and air-stabilization, Chem. Eng. J., 510 (2025) 161765 <a href="https://doi.org/10.1016/j.cej.2025.161765">https://doi.org/10.1016/j.cej.2025.161765</a>.
- [32] Y. Hua, M. Tan, M. Liu, X. Yu, D. Wang, Y. Liu, Medium-entropy P2-type layered metal oxide cathode demonstrating complete solid-solution behavior for improved Na-ion battery performance, J. Colloid Interface Sci., 695 (2025) 137744 <a href="https://doi.org/10.1016/j.jcis.2025.137744">https://doi.org/10.1016/j.jcis.2025.137744</a>.
- [33] Y. Ren, Q. Ge, Y. Wu, Q. Peng, J. Qian, X. Ding, A high-entropy cathode for sodiumion batteries: Cu/Zn-doping O3-Type Ni/Fe/Mn layer oxides, J. Phys. Chem. Solids, 194 (2024) 112241 <a href="https://doi.org/10.1016/j.jpcs.2024.112241">https://doi.org/10.1016/j.jpcs.2024.112241</a>.
- [34] X. Li, Y. Li, Q. Cui, M. Zhong, X. Zhao, J. Liu, Redox and structural stability for sodium-ion batteries through bond structure engineering, J. Mater. Chem. A, 12 (2024) 31145-31152 <a href="https://doi.org/10.1039/d4ta05924g">https://doi.org/10.1039/d4ta05924g</a>.
- [35] E. Gonzalo, L. Rodriguez-Castaño, Y. He, J.M.d.A. Añon, M. Galceran, A. Villaverde, M. Cabello, N.E. Drewett, Scalable synthesis of processable high performance O3-NaNi<sub>0.4</sub>Mn<sub>0.4</sub>Fe<sub>0.2</sub>O<sub>2</sub>: A methodological investigation and electrochemical insights, Electrochim. Acta, 536 (2025) 146738 <a href="https://doi.org/10.1016/j.electacta.2025.146738">https://doi.org/10.1016/j.electacta.2025.146738</a>.
- [36] S. Jia, M. Abdolhosseini, L. Saglio, Y. Li, M. Kamel, J.-D. Lavertu, S. Bazylevych, V. Saïbi, P.-E. Cabelguen, S. Kumakura, E. McCalla, High-throughput study examining the wide benefit of Li substitution in oxide cathodes for Na-ion batteries, Electrochim. Acta, 525 (2025) 146077 <a href="https://doi.org/10.1016/j.electacta.2025.146077">https://doi.org/10.1016/j.electacta.2025.146077</a>.
- [37] J. Liu, W. Qin, Z. Yang, Q. Liu, Y. Liu, Enhanced structural and cycling stability of O3-type NaNi<sub>1/3</sub>Mn<sub>1/3</sub>Fe<sub>1/3</sub>O<sub>2</sub> cathode by Al replacement of Mn studied in half cell/full sodiumion batteries, J. Alloys Compd., 933 (2023) 167714 <a href="https://doi.org/10.1016/j.jallcom.2022.167714">https://doi.org/10.1016/j.jallcom.2022.167714</a>.

- [38] A. Ma, Z. Yin, J. Wang, Z. Wang, H. Guo, G. Yan, Al-doped NaNi<sub>1/3</sub>Mn<sub>1/3</sub>Fe<sub>1/3</sub>O<sub>2</sub> for high performance of sodium ion batteries, Ionics, 26 (2020) 1797-1804 https://doi.org/10.1007/s11581-019-03437-z.
- [39] X. Liu, G. Zhong, Z. Xiao, B. Zheng, W. Zuo, K. Zhou, H. Liu, Z. Liang, Y. Xiang, Z. Chen, G.F. Ortiz, R. Fu, Y. Yang, Al and Fe-containing Mn-based layered cathode with controlled vacancies for high-rate sodium ion batteries, Nano Energy, 76 (2020) 104997 <a href="https://doi.org/10.1016/j.nanoen.2020.104997">https://doi.org/10.1016/j.nanoen.2020.104997</a>.
- [40] H.N. Vasavan, M. Badole, S. Saxena, V. Srihari, A.K. Das, P. Gami, N. Dagar, S. Deswal, P. Kumar, H.K. Poswal, S. Kumar, Identification of optimal composition with superior electrochemical properties along the zero Mn<sup>3+</sup> line in Na<sub>0.75</sub>(Mn-Al-Ni)O<sub>2</sub> pseudo ternary system, J. Energy Chem., 96 (2024) 206-216 <a href="https://doi.org/10.1016/j.jechem.2024.04.015">https://doi.org/10.1016/j.jechem.2024.04.015</a>.
- [41] N.V. Proskurnina, V.I. Voronin, G.S. Shekhtman, N.A. Kabanova, Crystal structure of NaFeO<sub>2</sub> and NaAlO<sub>2</sub> and their correlation with ionic conductivity, Ionics, 26 (2020) 2917-2926 https://doi.org/10.1007/s11581-019-03387-6.
- [42] S. Jia, J. Counsell, M. Adamič, A. Jonderian, E. McCalla, High-throughput design of Na–Fe–Mn–O cathodes for Na-ion batteries, J. Mater. Chem. A, 10 (2022) 251-265 <a href="https://doi.org/10.1039/D1TA07940A">https://doi.org/10.1039/D1TA07940A</a>.
- [43] S. Sun, X. Zhu, H. Dong, Y.-H. Feng, Y. Tang, M.-Y. Li, S.-W. Xu, H. Xin, C. Ma, G.-X. Wei, L.-J. Hu, H. Qin, M. Liu, Y. Xiao, B. Xiao, P.-F. Wang, P-Type Stacking Dominated Electrochemical Process Enables Fast Na<sup>+</sup> Transport for High-Energy P2/O3 Biphasic Cathodes, Adv. Funct. Mater., (2025) 2503900 <a href="https://doi.org/10.1002/adfm.202503900">https://doi.org/10.1002/adfm.202503900</a>.
- [44] E. Grépin, Q. Jacquet, I.A. Moiseev, A. Iadecola, G. Rousse, M. Avdeev, A.M. Abakumov, J.-M. Tarascon, S. Mariyappan, Mastering the synthesis of high Na-content, moisture-stable layered oxide cathode for Na-ion batteries, J. Power Sources, 613 (2024) 234962 <a href="https://doi.org/10.1016/j.jpowsour.2024.234962">https://doi.org/10.1016/j.jpowsour.2024.234962</a>.
- [45] Z. Liang, M. Ren, Y. Guo, T. Zhang, X. Gao, H. Ma, F. Li, Depressed P3–O3' phase transition in an O3-type layered cathode for advanced sodium-ion batteries, Inorg. Chem. Front., 10 (2023) 7187-7192 <a href="https://doi.org/10.1039/D3QI01884A">https://doi.org/10.1039/D3QI01884A</a>.
- [46] N. Ahmad, L. Yu, M.U. Muzaffar, B. Peng, Z. Tao, S. Khan, A. Rahman, J. Liang, Z. Jiang, X. Ma, G. Zhang, Dual-Pillar Effect in P2-Type Na<sub>0.67</sub>Ni<sub>0.33</sub>Mn<sub>0.67</sub>O<sub>2</sub> Through Na Site

- Substitution Achieve Superior Electrochemical and Air/Water Dual-Stability as Cathode for Sodium-Ion Batteries, Adv. Energy Mater., 15 (2025) 2404093 <a href="https://doi.org/10.1002/aenm.202404093">https://doi.org/10.1002/aenm.202404093</a>.
- [47] T. Song, L. Chen, D. Gastol, B. Dong, J.F. Marco, F. Berry, P. Slater, D. Reed, E. Kendrick, High-Voltage Stabilization of O3-Type Layered Oxide for Sodium-Ion Batteries by Simultaneous Tin Dual Modification, Chem. Mater., 34 (2022) 4153-4165 <a href="https://doi.org/10.1021/acs.chemmater.2c00522">https://doi.org/10.1021/acs.chemmater.2c00522</a>.
- [48] Z.-C. Jian, W. Shi, Y. Liu, X. Li, J. Li, Y.-F. Zhu, X. Zhu, Y. Li, P. Tan, P.-F. Wang, S. Chen, S. Zhang, J. Mao, G. Zhou, X. Guo, J. Wang, S.-X. Dou, Y. Xiao, Accelerating lattice oxygen kinetics of layered oxide cathodes via active facet modulation and robust mechanochemical interface construction for high-energy-density sodium-ion batteries, Energy Environ. Sci., 18 (2025) 7995-8008 <a href="https://doi.org/10.1039/D5EE00467E">https://doi.org/10.1039/D5EE00467E</a>.
- [49] W. Xiong, Z. Liu, W. Cheng, J. Zheng, Y. Zou, X. Chen, Y. Liu, Facilitating the oxygen redox chemistry in O3-type layered oxide cathode material for sodium-ion batteries by Fe substitution, J. Energy Chem., 103 (2025) 59-67 <a href="https://doi.org/10.1016/j.jechem.2024.10.058">https://doi.org/10.1016/j.jechem.2024.10.058</a>.
- [50] L. Zhou, M. Yang, J. Meng, F. Wang, C. Chen, D. Fu, Y. Zhong, T. Sun, W. Hu, Q. Ma, Construction of oxygen vacancies enables a highly stable Li-rich layered oxides via nitrogen assisted roasting, J. Power Sources, 641 (2025) 236803 <a href="https://doi.org/10.1016/j.jpowsour.2025.236803">https://doi.org/10.1016/j.jpowsour.2025.236803</a>.
- [51] Z.-Y. Li, J. Zhang, R. Gao, H. Zhang, L. Zheng, Z. Hu, X. Liu, Li-Substituted Co-Free Layered P2/O3 Biphasic Na<sub>0.67</sub>Mn<sub>0.55</sub>Ni<sub>0.25</sub>Ti<sub>0.2-x</sub>Li<sub>x</sub>O<sub>2</sub> as High-Rate-Capability Cathode Materials for Sodium Ion Batteries, J. Phys. Chem. C, 120 (2016) 9007-9016 <a href="https://doi.org/10.1021/acs.jpcc.5b11983">https://doi.org/10.1021/acs.jpcc.5b11983</a>.
- [52] S.-M. Oh, S.-T. Myung, J.-Y. Hwang, B. Scrosati, K. Amine, Y.-K. Sun, High Capacity O3-Type Na[Li<sub>0.05</sub>(Ni<sub>0.25</sub>Fe<sub>0.25</sub>Mn<sub>0.5</sub>)<sub>0.95</sub>]O<sub>2</sub> Cathode for Sodium Ion Batteries, Chem. Mater., 26 (2014) 6165-6171 <a href="https://doi.org/10.1021/cm502481b">https://doi.org/10.1021/cm502481b</a>.
- [53] X. Rong, X. Qi, Y. Lu, Y. Wang, Y. Li, L. Jiang, K. Yang, F. Gao, X. Huang, L. Chen, Y.-S. Hu, A new Tin-based O3-Na<sub>0.9</sub>[Ni<sub>0.45-x/2</sub>Mn<sub>x</sub>Sn<sub>0.55-x/2</sub>]O<sub>2</sub> as sodium-ion battery cathode, J. Energy Chem., 31 (2019) 132-137 <a href="https://doi.org/10.1016/j.jechem.2018.05.019">https://doi.org/10.1016/j.jechem.2018.05.019</a>.

- [54] P. Wen, H. Shi, D. Guo, A. Wang, Y. Yu, Z.-S. Wu, Ti, F Codoped Sodium Manganate of Layered P2-Na<sub>0.7</sub>MnO<sub>2.05</sub> Cathode for High Capacity and Long-Life Sodium-Ion Battery, Renewables, 1 (2023) 81-89 https://doi.org/10.31635/renewables.022.202200012.
- [55] I.B. Slima, K. Moufida, F. Missaoui, L. Fkhar, A. Mahmoud, A.B. Rhaiem, Conduction mechanism and electrochemical properties of P2-Na<sub>2/3</sub>Fe<sub>1/3</sub>Mn<sub>2/3</sub>O<sub>2</sub> for Na-ion batteries, J. Am. Ceram. Soc., 108 (2025) e20707 <a href="https://doi.org/10.1111/jace.20707">https://doi.org/10.1111/jace.20707</a>.
- [56] H. Maejima, T. Hosaka, R. Tatara, K. Kubota, Y. Tokita, M. Goktas, P. Adelhelm, S. Komaba, A Sodium-Ion Battery with the Diglyme Electrolyte: Graphite || Alumina-Coated Na<sub>5/6</sub>[Ni<sub>1/3</sub>Mn<sub>1/6</sub>Fe<sub>1/6</sub>Ti<sub>1/3</sub>]O<sub>2</sub> Cell, Chem. Mater., 37 (2025) 5052-5061 https://doi.org/10.1021/acs.chemmater.5c00541.
- [57] L. Marti, M. Canini, M. Ravalli, M.C. Mozzati, M.B. Maccioni, A. Floris, P. Galinetto, E. Quartarone, M. Cococcioni, C. Tealdi, Intercalation voltages and ion diffusion in Mn-based transition metal fluorophosphates as cathode materials for Na-ion batteries: a synergistic experimental and theoretical approach, J. Energy Storage, 127 (2025) 117143 https://doi.org/10.1016/j.est.2025.117143.
- [58] H. He, D. Sun, Y. Tang, H. Wang, M. Shao, Understanding and improving the initial Coulombic efficiency of high-capacity anode materials for practical sodium ion batteries, Energy Storage Mater., 23 (2019) 233-251 <a href="https://doi.org/10.1016/j.ensm.2019.05.008">https://doi.org/10.1016/j.ensm.2019.05.008</a>.
- [59] Y. Li, K.A. Mazzio, N. Yaqoob, Y. Sun, A.I. Freytag, D. Wong, C. Schulz, V. Baran, A.S.J. Mendez, G. Schuck, M. Zając, P. Kaghazchi, P. Adelhelm, Competing Mechanisms Determine Oxygen Redox in Doped Ni–Mn Based Layered Oxides for Na-Ion Batteries, Adv. Mater., 36 (2024) 2309842 <a href="https://doi.org/10.1002/adma.202309842">https://doi.org/10.1002/adma.202309842</a>.
- [60] Z. Lu, J.R. Dahn, In Situ X-Ray Diffraction Study of P2 Na<sub>2/3</sub> [Ni<sub>1/3</sub>Mn<sub>2/3</sub>]O<sub>2</sub>, J. Electrochem. Soc., 148 (2001) A1225 <a href="https://doi.org/10.1149/1.1407247">https://doi.org/10.1149/1.1407247</a>.
- [61] R.J. Clément, P.G. Bruce, C.P. Grey, Review—Manganese-Based P2-Type Transition Metal Oxides as Sodium-Ion Battery Cathode Materials, J. Electrochem. Soc., 162 (2015) A2589 https://doi.org/10.1149/2.0201514jes.
- [62] Q. Wang, G. Yu, B. Luo, W. Ji, Z. Liu, M. Li, Y. Nong, Y. Tian, X. Wang, J. Zhang, C.-L. Chen, C.-K. Chang, Z. Sang, Z. Zhao, R. Zhao, J. Liang, Suppression of Adverse Phase Transition of Layered Oxide Cathode via Local Electronic Structure Regulation for High-

- Capacity Sodium-Ion Batteries, ACS Nano, 18 (2024) 18622-18634 <a href="https://doi.org/10.1021/acsnano.4c04847">https://doi.org/10.1021/acsnano.4c04847</a>.
- [63] R. Li, Y. Liu, Z. Wang, J. Li, A P2/O3 biphasic cathode material with highly reversibility synthesized by Sn-substitution for Na-ion batteries, Electrochim. Acta, 318 (2019) 14-22 <a href="https://doi.org/10.1016/j.electacta.2019.06.020">https://doi.org/10.1016/j.electacta.2019.06.020</a>.
- [64] E. Lee, J. Lu, Y. Ren, X. Luo, X. Zhang, J. Wen, D. Miller, A. DeWahl, S. Hackney, B. Key, D. Kim, M.D. Slater, C.S. Johnson, Layered P2/O3 Intergrowth Cathode: Toward High Power Na-Ion Batteries, Adv. Energy Mater., 4 (2014) 1400458 <a href="https://doi.org/10.1002/aenm.201400458">https://doi.org/10.1002/aenm.201400458</a>.
- [65] T.-Y. Yu, H.-H. Ryu, G. Han, Y.-K. Sun, Understanding the Capacity Fading Mechanisms of O3-Type Na[Ni<sub>0.5</sub>Mn<sub>0.5</sub>]O<sub>2</sub> Cathode for Sodium-Ion Batteries, Adv. Energy Mater., 10 (2020) 2001609 <a href="https://doi.org/10.1002/aenm.202001609">https://doi.org/10.1002/aenm.202001609</a>.
- [66] X. Zhao, L. Hou, Q. Liu, Y. Zhao, D. Mu, Z. Zhao, L. Li, R. Chen, F. Wu, Insights into the capacity fading and failure mechanism of an O3-NaNi<sub>1/3</sub>Fe<sub>1/3</sub>Mn<sub>1/3</sub>O<sub>2</sub> layered oxide cathode material for sodium-ion batteries, J. Mater. Chem. A, 12 (2024) 12443-12451 https://doi.org/10.1039/D4TA00060A.
- [67] A.R.C. Bredar, A.L. Chown, A.R. Burton, B.H. Farnum, Electrochemical Impedance Spectroscopy of Metal Oxide Electrodes for Energy Applications, ACS Appl. Energy Mater., 3 (2020) 66-98 <a href="https://doi.org/10.1021/acsaem.9b01965">https://doi.org/10.1021/acsaem.9b01965</a>.
- [68] L. Wang, J. Zhao, X. He, J. Gao, J. Li, C. Wan, C. Jiang, Electrochemical Impedance Spectroscopy (EIS) Study of LiNi1/3Co<sub>1/3</sub>Mn<sub>1/3</sub>O<sub>2</sub> for Li-ion Batteries, Int. J. Electrochem. Sci., 7 (2012) 345-353 <a href="https://doi.org/10.1016/S1452-3981(23)13343-8">https://doi.org/10.1016/S1452-3981(23)13343-8</a>.
- [69] L. Minnetti, L. Sbrascini, A. Staffolani, V. Marangon, F. Nobili, J. Hassoun, Unravelling the ion transport and the interphase properties of a mixed olivine cathode for Na-ion battery, J. Energy Chem., 96 (2024) 300-317 https://doi.org/10.1016/j.jechem.2024.04.028.
- [70] J. Chen, E. Quattrocchi, F. Ciucci, Y. Chen, Charging processes in lithium-oxygen batteries unraveled through the lens of the distribution of relaxation times, Chem, 9 (2023) 2267-2281 <a href="https://doi.org/10.1016/j.chempr.2023.04.022">https://doi.org/10.1016/j.chempr.2023.04.022</a>.
- [71] Y. Lu, C.-Z. Zhao, J.-Q. Huang, Q. Zhang, The timescale identification decoupling complicated kinetic processes in lithium batteries, Joule, 6 (2022) 1172-1198 <a href="https://doi.org/10.1016/j.joule.2022.05.005">https://doi.org/10.1016/j.joule.2022.05.005</a>.

- [72] S. Bakenhaster, H. Dewald, Electrochemical impedance spectroscopy and battery systems: past work, current research, and future opportunities, J. Appl. Electrochem., 55 (2025) 1657-1681 <a href="https://doi.org/10.1007/s10800-025-02273-6">https://doi.org/10.1007/s10800-025-02273-6</a>.
- [73] Y. Li, A. Feng, T. Yang, N. Chen, A. Li, Y. Yang, R. Liu, L. Zhang, X. Qin, Enhanced stability in a layered P2-Na<sub>0.67</sub>Fe<sub>0.5</sub>Mn<sub>0.5</sub>O<sub>2</sub> cathode for sodium ion batteries via a synergistic Cu/Ti co-doping strategy, Inorg. Chem. Front., (2025) <a href="http://dx.doi.org/10.1039/D5QI01070E">http://dx.doi.org/10.1039/D5QI01070E</a>.
- [74] X. Liang, X. Song, H.H. Sun, H. Kim, M.-C. Kim, Y.-K. Sun, High-energy and long-life O3-type layered cathode material for sodium-ion batteries, Nat. Commun., 16 (2025) 3505 <a href="https://doi.org/10.1038/s41467-025-58637-1">https://doi.org/10.1038/s41467-025-58637-1</a>.
- [75] J. Lamb, L. Stokes, A. Manthiram, Delineating the Capacity Fading Mechanisms of Na(Ni<sub>0.3</sub>Fe<sub>0.4</sub>Mn<sub>0.3</sub>)O<sub>2</sub> at Higher Operating Voltages in Sodium-Ion Cells, Chem. Mater., 32 (2020) 7389-7396 10.1021/acs.chemmater.0c02292.
- [76] X. Zhao, Q. Liu, W. He, D. Mu, L. Li, R. Chen, F. Wu, Uniform Al<sub>2</sub>O<sub>3</sub> coating for improved cycling stability of O3-type sodium-ion batteries cathode: Mechanisms and performance insights, J. Energy Storage, 131 (2025) 117548

  <a href="https://doi.org/10.1016/j.est.2025.117548">https://doi.org/10.1016/j.est.2025.117548</a>.
- [77] Q. Zhang, Q.-F. Gu, Y. Li, H.-N. Fan, W.-B. Luo, H.-K. Liu, S.-X. Dou, Surface Stabilization of O3-type Layered Oxide Cathode to Protect the Anode of Sodium Ion Batteries for Superior Lifespan, iScience, 19 (2019) 244-254 <a href="https://doi.org/10.1016/j.isci.2019.07.029">https://doi.org/10.1016/j.isci.2019.07.029</a>.

## [Supplementary Materials]

# Synthesis, Structure, and Electrochemical Behaviour of O3-type $NaNi_{1/3}Mn_{1/3}Al_{1/3}O_2$

Neha Dagar<sup>1</sup>, Samriddhi Saxena<sup>1</sup>, Sonia Deswal<sup>2</sup>, Pradeep Kumar<sup>2</sup>, Karthik Chinnathambi<sup>3</sup>, and Sunil Kumar<sup>1,\*</sup>

<sup>1</sup>Department of Metallurgical Engineering and Materials Science, Indian Institute of Technology Indore, Simrol, 453552, India

<sup>2</sup>School of Physical Sciences, Indian Institute of Technology Mandi, Mandi, 175005, India <sup>3</sup>Micron School of Materials Science and Engineering, Boise State University, Boise, ID 83725, USA

\*sunil@iiti.ac.in

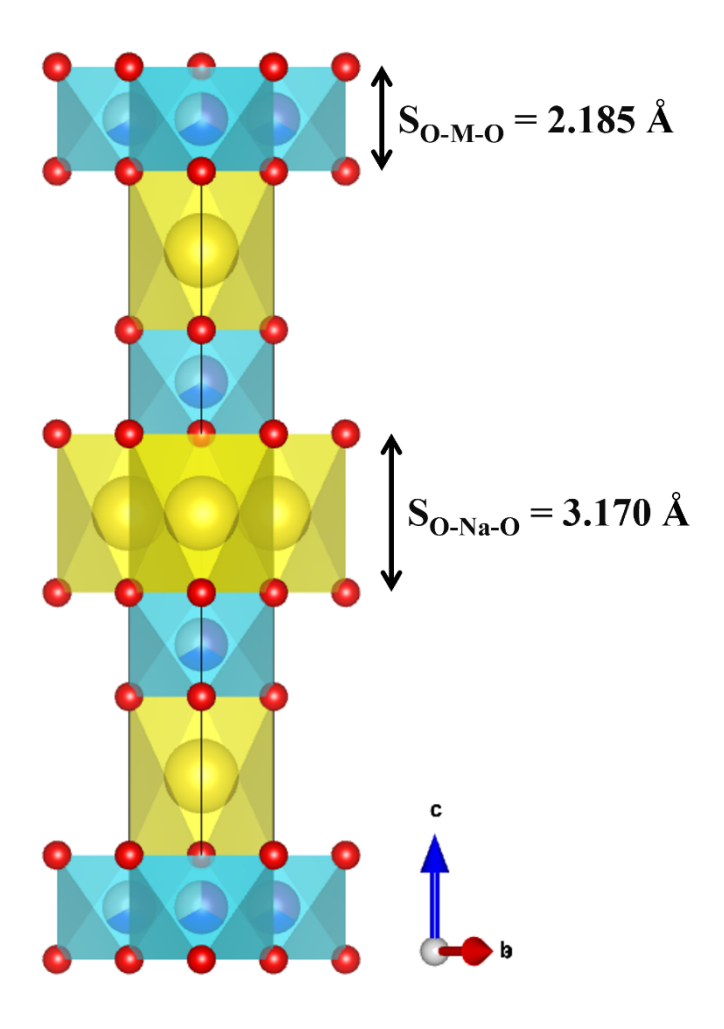
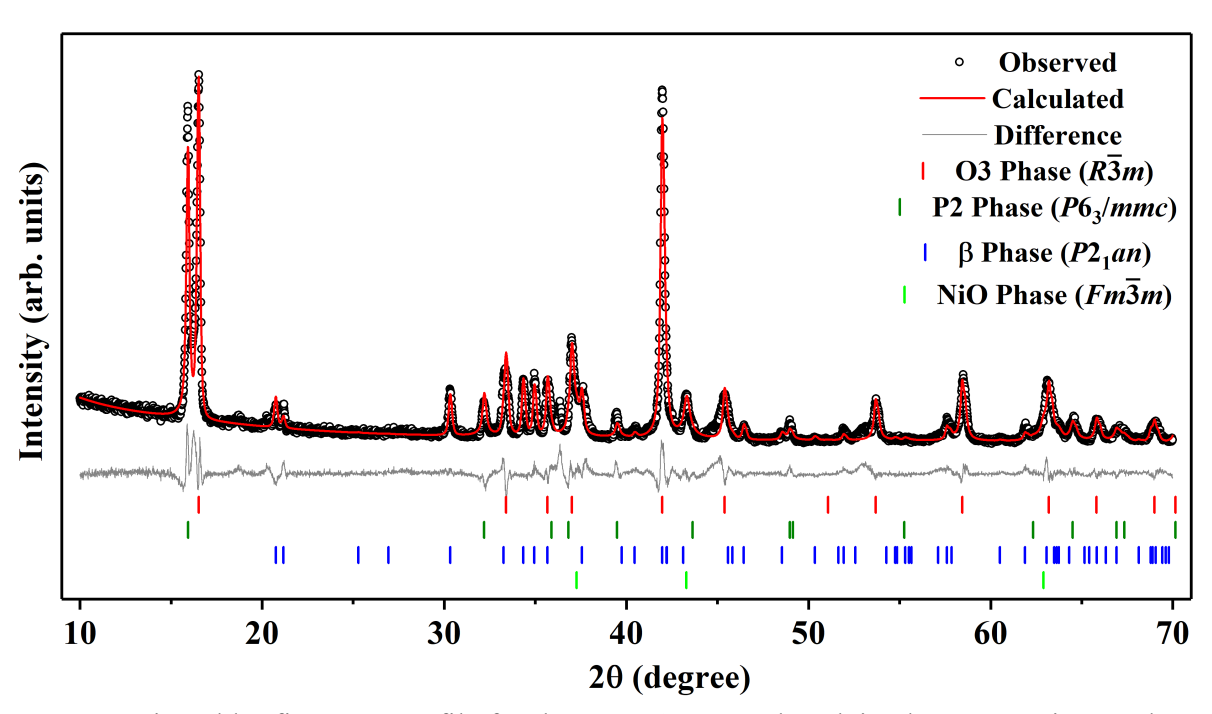
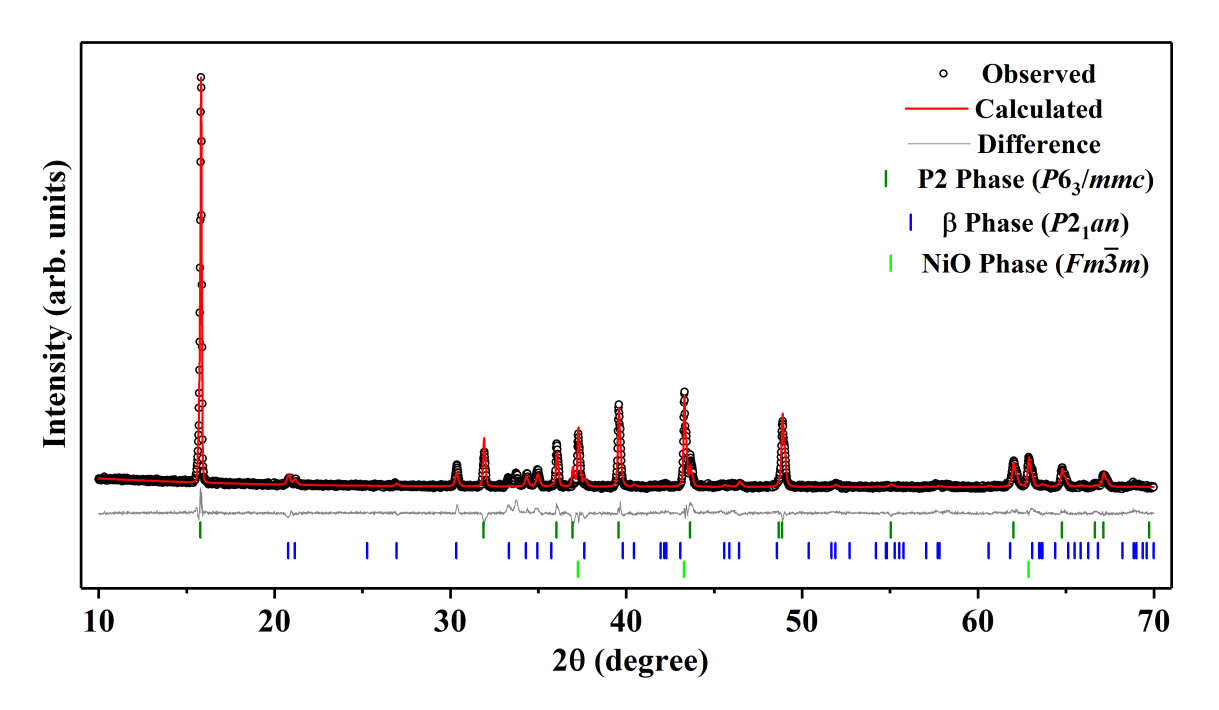


Fig. S1. Schematics of O3-type NMA111 structure.



**Fig. S2.** Rietveld refinement profile for the NMA111 sample calcined at 850 °C in powder form (Powder-850).



**Fig. S3.** Rietveld refinement profile for the NMA111 sample calcined at 1000 °C in powder form (Powder-1000).

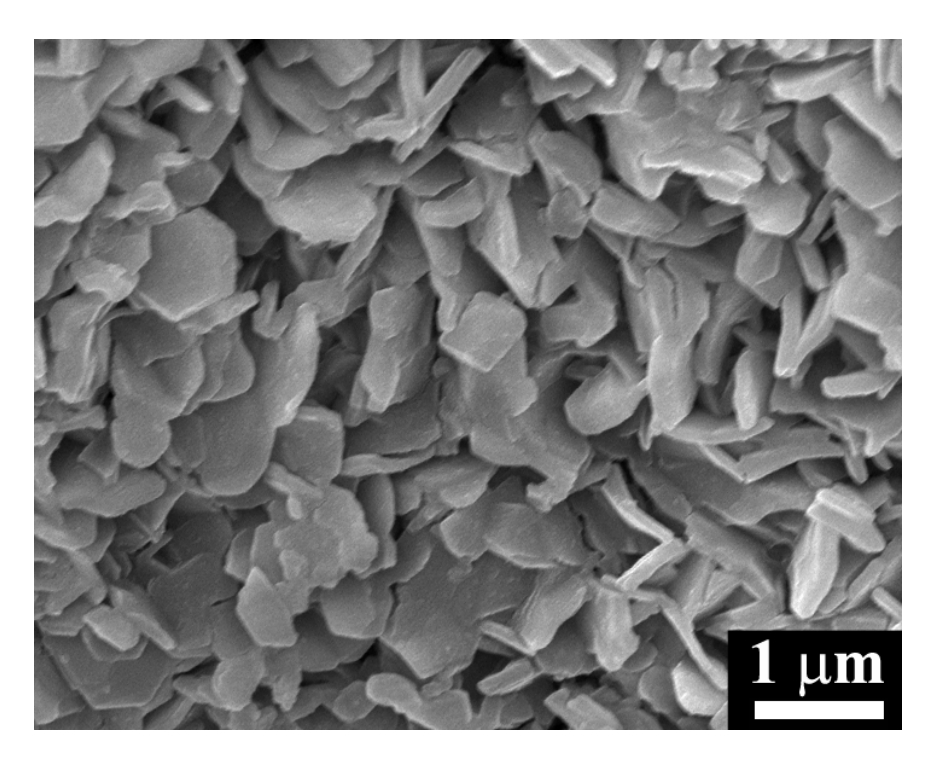
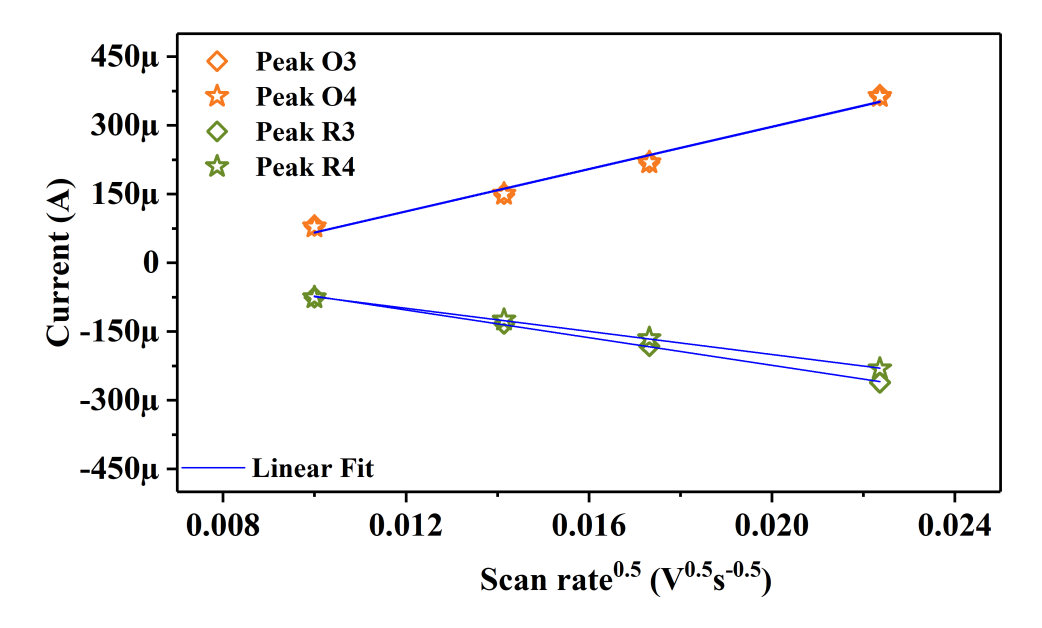


Fig. S4. SEM images of NMA111 sacrificial powder heated at 850 °C.



**Fig. S5.** Linear relationship of peak currents with the square root of scan rate for different peaks.

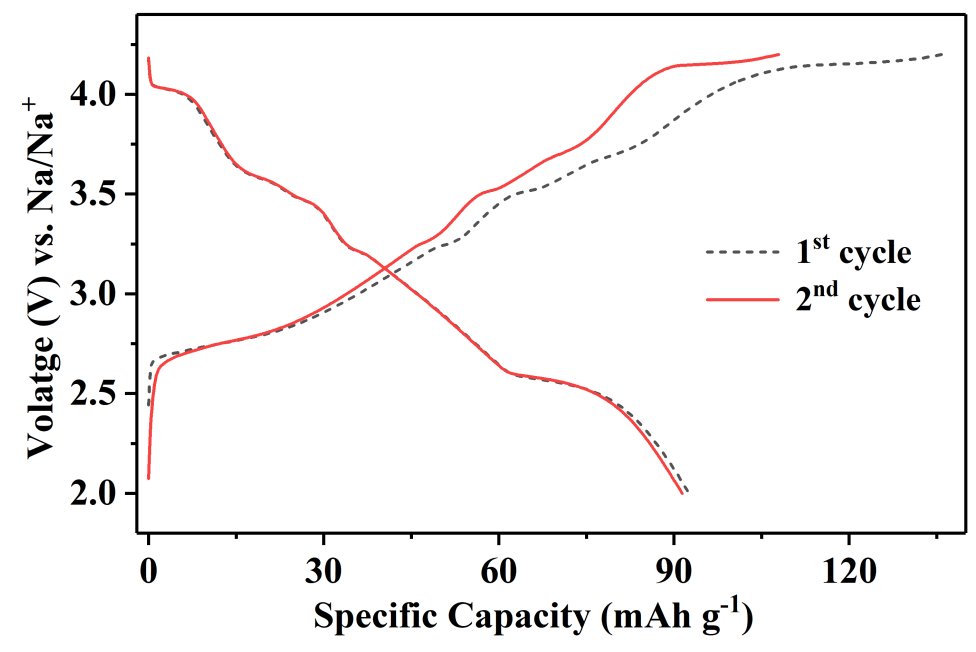


Fig. S6.  $1^{st}$  two charge-discharge cycles of NMA111 (Pellet-850) at 0.1C cycled between 2.0 V and 4.2 V.

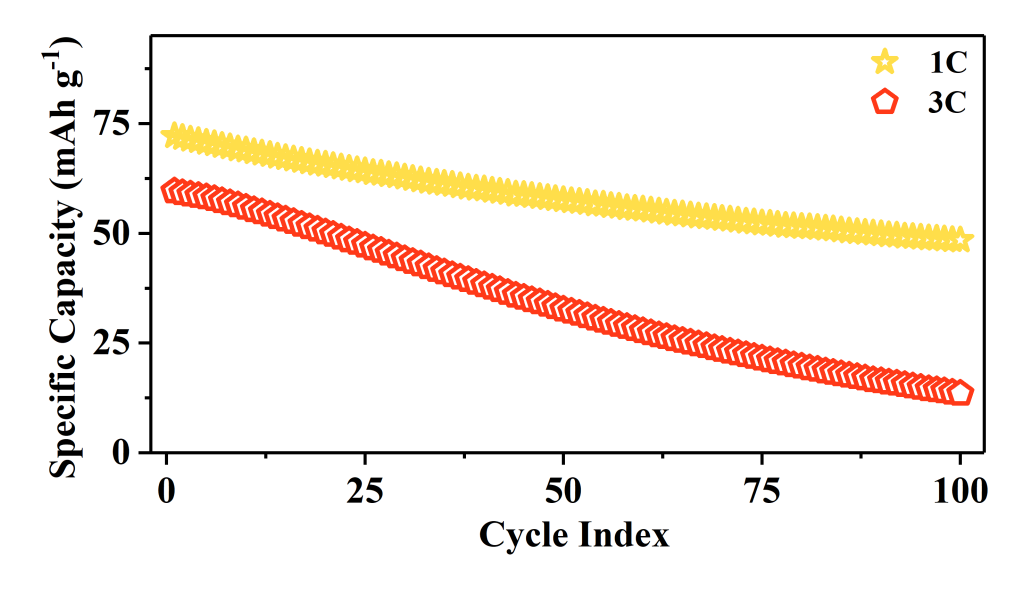
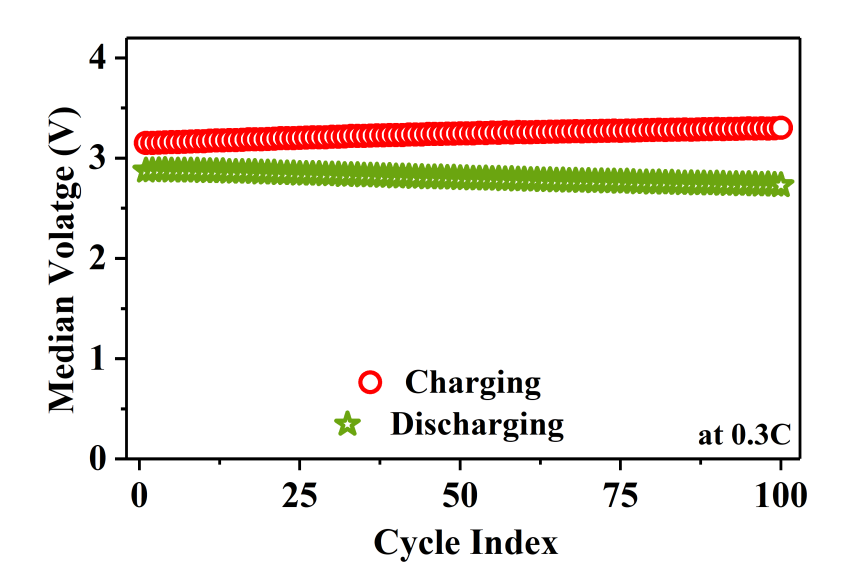
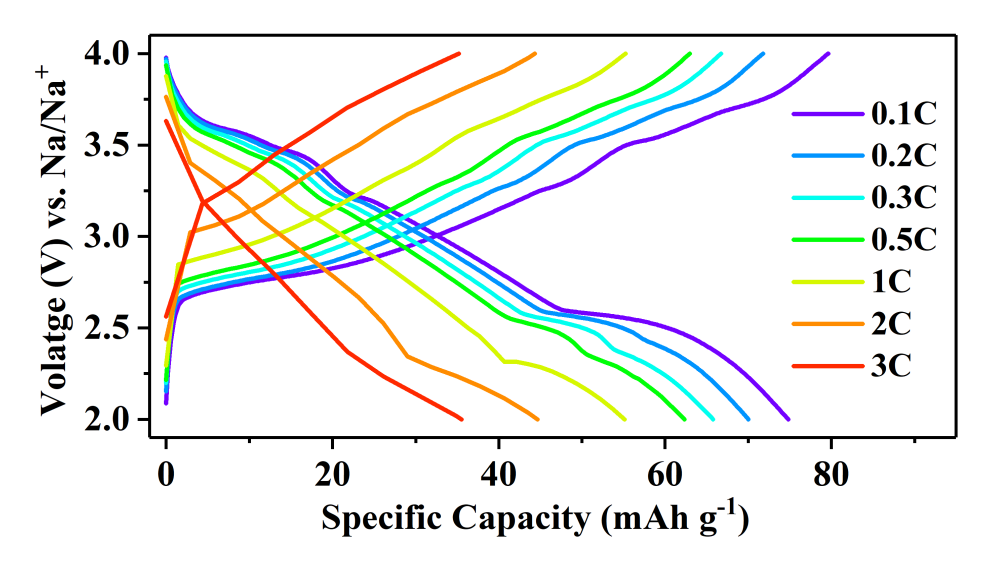


Fig. S7: The cyclability of the NMA111 cathode (Pellet-850) at 1C and 3C.



**Fig. S8.** Median charging and discharging voltage of the NMA111 cathode (Pellet-850) for various cycles at 0.3C.



**Fig. S9.** The GCD behavior of the NMA111 cathode prepared from sacrificial powder (Powder-850) at various C rates.

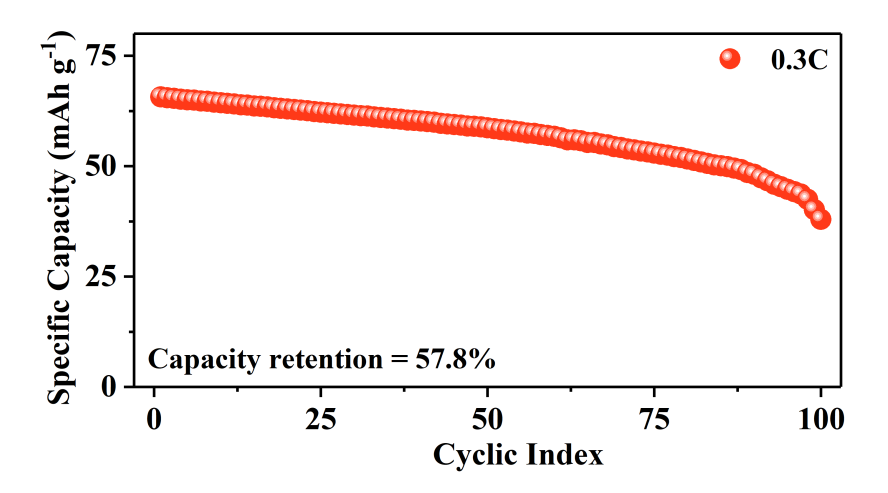


**Fig. S10:** The cyclability of the NMA111 cathode prepared from sacrificial powder (Powder-850) at 0.3C.

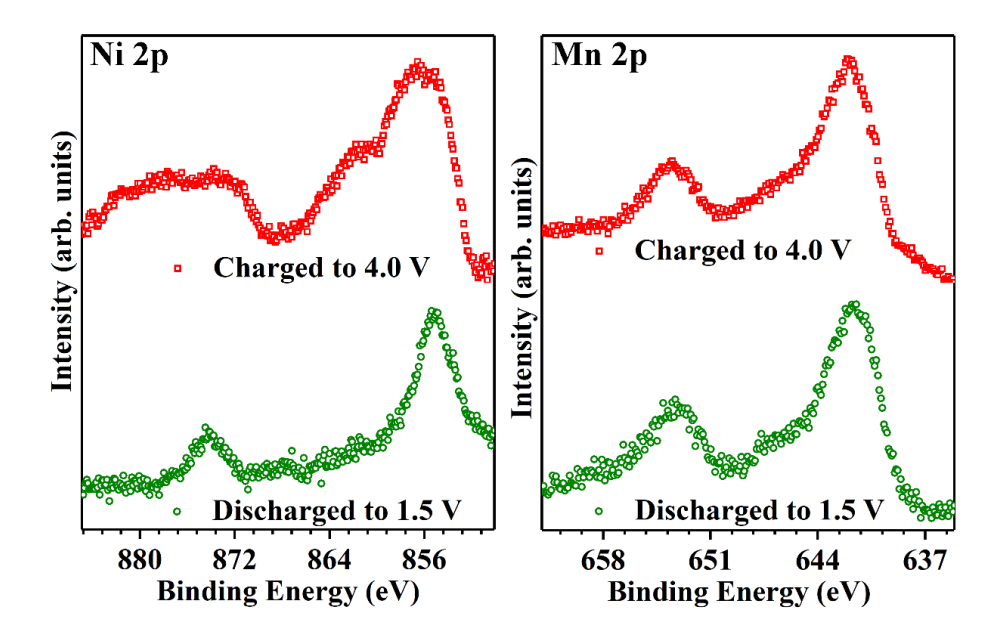


**Fig. S11.** Ex situ Ni 2p and Mn 2p XPS data for NMA111 cathode charged to 4.0 V and discharged to 1.5V.

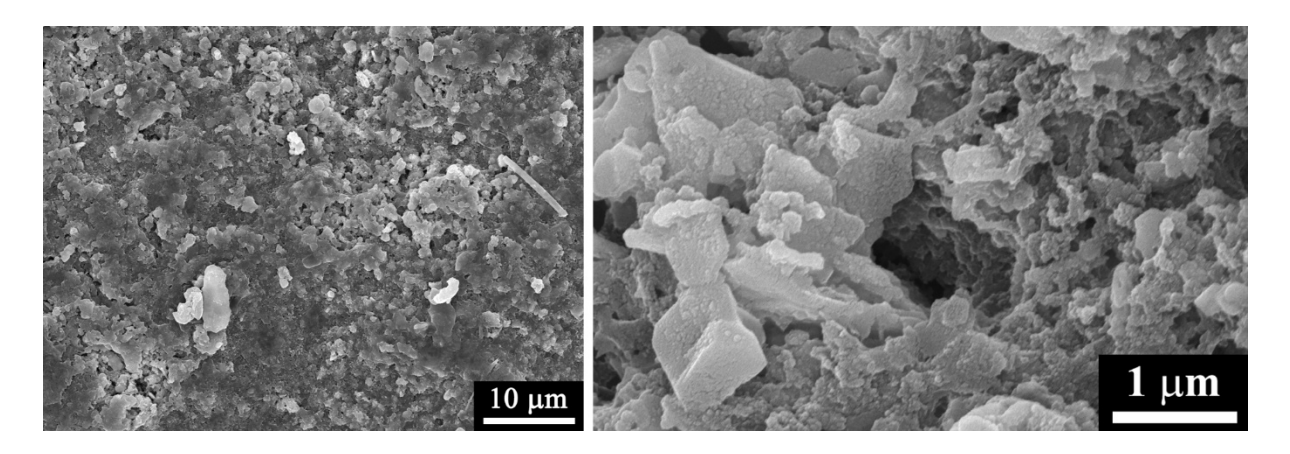


**Fig. S12.** The SEM images of the cycled NMA111 (Pellet-850) cathode at different magnifications.

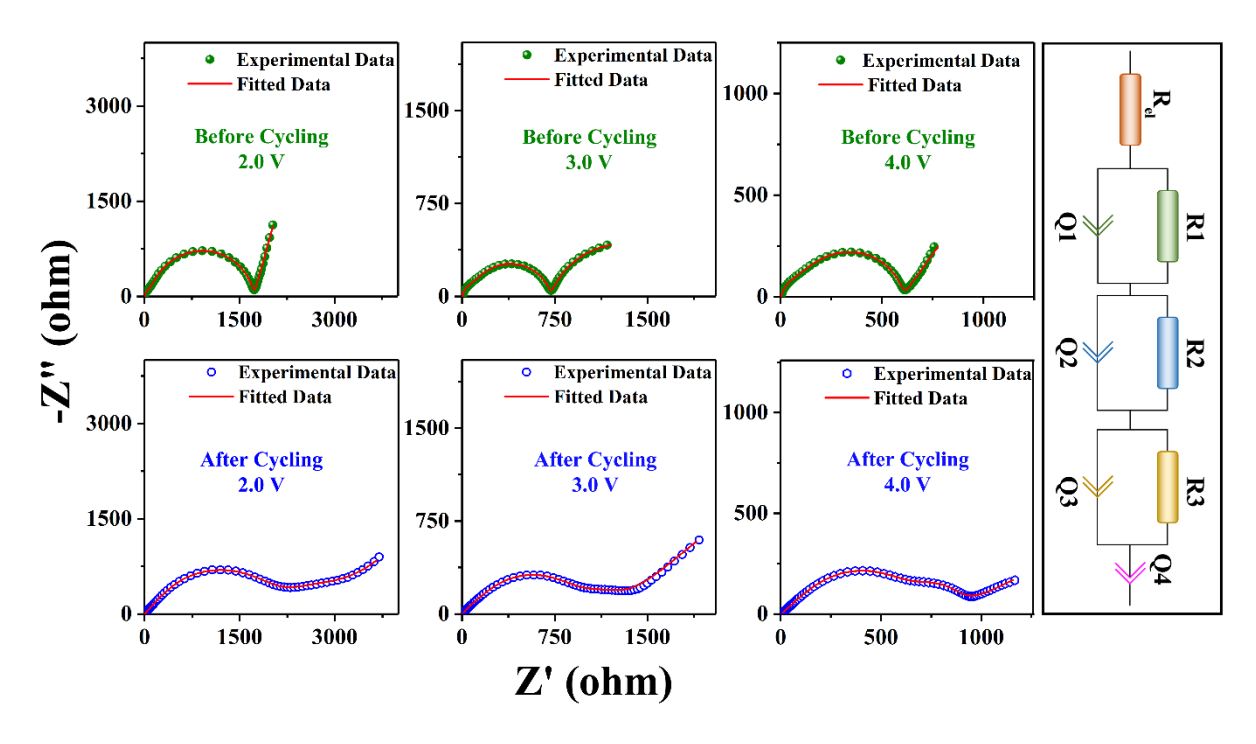


**Fig. S13.** Nyquist plot of NMA111 half-cell (Pellet-850 cathode) before and after cycling for 100 cycles at 0.3C, along with the equivalent circuit used for fitting (shown in rightmost panel). The circuit element R<sub>el</sub> represents the electrolyte resistance, R1 & R2 represent the interphase layers' resistance, R3 represents charge-transfer resistance, and Q4 reflects the diffusion process in solid cathode particles.

**Table S1:** Various structural parameters obtained from the Rietveld refinement of room temperature powder x-ray diffraction data for the NMA111 pellet sample heated at 850 °C (Pellet-850). x, y, z — positional coordinates along with the fitness parameters (Rexp, Rwp, Rp, and goodness of fit – GoF).

		Atom	x	у	z	Occupancy
	03	Na	0	0	0.5	1
	03	Ni/Mn/Al	0	0	0	0.333/0.334/0.333
		O	0	0	0.265	1
$R_{exp} = 7.00$	_	Nae	2/3	1/3	1/4	0.65
$R_{wp} = 9.54$	P2 -	$Na_{\mathrm{f}}$	0	0	1/4	0.35
$R_p = 7.24$	1 2	Ni/ Mn/ Al	0	0	0	0.333/0.334/0.333
GOF = 1.36		O	2/3	1/3	0.08	1
	_	Na	0.416	0.520	0.142	1
	0	Ni/ Mn/ Al	0.060	0	0.141	0.333/0.334/0.333
	β -	O1	0.05	0.678	0.08	1
	_	O2	0.380	0.080	0.128	1

**Table S2:** The weight (%) of various elements in NMA111 samples determined from the ICP-OES measurements.

Sample	Na (wt.%)	Ni (wt.%)	Mn (wt.%)	Al (wt.%)	Chemical Composition
Expected	32.91	28.01	26.22	12.87	$NaNi_{1/3}Mn_{1/3}Al_{1/3}O_2 \\$
Pellet-850	31.82	28.21	26.81	13.17	$Na_{0.95}Ni_{0.330}Mn_{0.335}Al_{0.335}O_2$
Powder-850	28.77	29.14	28.08	14.00	$Na_{0.82}Ni_{0.325}Mn_{0.335}Al_{0.340}O_2$

**Table S3**: Refined structural parameters for  $NaMn_{1/3}Al_{1/3}Ni_{1/3}O_2$  powder calcined at 850 °C (Powder-850).

Powder-850	O3 phase	P2 phase	β phase	NiO Phase
Crystal system	Rhombohedral	Hexagonal	Orthorhombic	Cubic
Space group	$R\overline{3}m$	P6 <sub>3</sub> /mmc	$Pn2_1a$	$Fm\overline{3}m$
Phase fractions	55%	32%	6.9%	6.1%
Cell Parameters, Å				
	a = 2.9401(7)	a = 2.8870(4)	a = 5.3854(8)	a = 4.1762(6)
			b = 5.2190(5)	
	c = 16.085(1)	c = 11.114(1)	c = 7.037(1)	
Cell Volume <i>V</i> , Å <sup>3</sup>	120.42(1)	80.23(2)	197.80(4)	72.836(3)

**Table S4:** Various structural parameters obtained from the Rietveld refinement of room temperature powder x-ray diffraction data for the NMA111 sacrificial powder heated at 850 °C (Powder-850). x, y, z — positional coordinates along with the fitness parameters (Rexp, Rwp, Rp, and goodness of fit – GoF).

		Atom	x	y	z	Occupancy
	03	Na	0	0	0.5	1
	O3	Ni/Mn/Al	0	0	0	0.333/0.334/0.333
		О	0	0	0.259	1
		Na <sub>e</sub>	2/3	1/3	1/4	0.65
$R_{exp} = 6.84$	D2	$Na_{\mathrm{f}}$	0	0	1/4	0.35
$R_{wp} = 15.01$	P2	Ni/ Mn/ Al	0	0	0	0.333/0.334/0.333
$R_p = 10.96$		О	2/3	1/3	0.09	1
GOF = 2.19		Na	0.415	0.520	0.108	1
	0	Ni/ Mn/ Al	0.090	0	0.144	0.333/0.334/0.333
	β	O1	0.049	0.57	0.08	1
		O2	0.362	0.080	0.188	1
	NiO	Ni	0	0	0	1
	NiO	0	1/2	1/2	1/2	1

**Table S5**: Refined structural parameters for NaMn<sub>1/3</sub>Al<sub>1/3</sub>Ni<sub>1/3</sub>O<sub>2</sub> powder calcined at 1000 °C (Powder-1000).

Powder-1000	P2 phase	β phase	NiO Phase
Crystal system	Hexagonal	Orthorhombic	Cubic
Space group	$P6_3/mmc$	$Pn2_1a$	$Fm\overline{3}m$
Phase fractions	70%	11%	19%
Cell Parameters, Å			
	a = 2.876(1)	a = 5.3722(1)	a = 4.1767(8)
		b = 5.2255(9)	
	c = 11.2160(5)	c = 7.0424(1)	
Cell Volume V, Å <sup>3</sup>	80.343(7)	197.70(7)	72.865(6)

**Table S6:** Various structural parameters obtained from the Rietveld refinement of room temperature powder x-ray diffraction data for the NMA111 sample heated at  $1000 \,^{\circ}$ C in powder form (Powder-1000). x, y, z — positional coordinates along with the fitness parameters (Rexp, Rwp, Rp, and goodness of fit – GoF).

		Atom	x	у	z	Occupancy
		Na <sub>e</sub>	2/3	1/3	1/4	0.65
	P2	Na <sub>f</sub>	0	0	1/4	0.35
	(70%)	Ni/ Mn/ Al	0	0	0	0.333/0.334/0.333
$R_{exp} = 2.47$		О	2/3	1/3	0.078	1
$R_{wp} = 5.49$ $R_p = 3.56$		Na	0.416	0.520	0.142	1
GOF = 2.22	β	Ni/ Mn/ Al	0.169	0	0.147	0.333/0.334/0.333
2.22	(11%)	O1	0.05	0.678	0.08	1
		O2	0.380	0.080	0.128	1
	NiO	Ni	0	0	0	1
	(19%)	О	1/2	1/2	1/2	1

**Table S7:** The values of various parameters obtained from equivalent circuit modeling of impedance data for the NMA111 pellet (Pellet-850).

	Pellet-850	Fitted Value ± Error
	$R_{G}(k\Omega)$	$57.9 \pm 0.2$
	$R_{GB}(k\Omega)$	$44.0 \pm 0.2$
O.c.	$Q(s^n/\Omega)$	$(1.85 \pm 0.07) \times 10^{-9}$
Q <sub>G</sub>	n	$0.75 \pm 0.01$
0	$Q(s^n/\Omega)$	$(1.61 \pm 0.08) \times 10^{-7}$
$Q_{GB}$	n	$0.66 \pm 0.02$
0	$Q(s^n/\Omega)$	$(2.4 \pm 0.2) \times 10^{-5}$
$\mathbf{Q}_{\mathrm{EL}}$	n	$0.36 \pm 0.08$